1 # Revision 1

2 # Amphibole-rich cumulate xenoliths in the Zhazhalong intrusive suite,

3 # Gangdese arc: Implications for the role of amphibole fractionation

4 # during magma evolution

5

6 JIN-SHENG ZHOU[1, 2, *], ZHU-SEN YANG[3], ZENG-QIAN HOU[1], AND QIANG

7 WANG[2, 4, 5]

8

9 [1]Institute of Geology, Chinese Academy of Geological Sciences, Beijing 100037, China

10 [2]State Key Laboratory of Isotope Geochemistry, Guangzhou Institute of Geochemistry, Chinese Academy of

11 Sciences, Guangzhou 510640, China

12 [3]MLR Key Laboratory of Metallogeny and Mineral Assessment, Institute of Mineral Resources, CAGS,

13 Beijing, 100037, China

14 [4]CAS Center for Excellence in Tibetan Plateau Earth Sciences, Beijing 100101, China

15 [5]College of Earth and Planetary Sciences, University of Chinese Academy of Sciences, Beijing 10049, China

16

17

18 * Present address: State Key Laboratory of Isotope Geochemistry, Guangzhou Institute of Geochemistry,

19 Chinese Academy of Sciences, Guangzhou 510640, China. E-mail: jinshengzhou@gig.ac.cn

20

21

22   **ABSTRACT**

23   Amphibole fractionation during the early evolution of arc magmas has been widely inferred

24   on the basis of distinctive geochemical fingerprints of the evolved melts, although amphibole is

25   rarely found as a major mineral phase in arc volcanic rocks, so-called cryptic amphibole

26   fractionation. Here, we present a detailed case study of xenoliths of amphibole-rich cumulate

27   from the Zhazhalong intrusive suite, Gangdese arc, which enable an investigation of this

28   differentiation process using a combination of petrological observations and in situ geochemical

29   constraints. Evidence that the xenoliths represent fragments of igneous cumulates includes: (i) the

30   presence of an amphibole-dominated crystal framework; (ii) mineral and whole-rock Fe–Mg

31   exchange coefficients; (iii) rare-earth element patterns that are similar in the amphiboles and the

32   xenoliths; (iv) the compositions of basaltic to andesitic liquids in equilibrium with amphiboles;

33   and (v) enrichment of the xenoliths in compatible elements and depletion in incompatible

34   elements. The amount of trapped liquid based on La, Ce and Dy abundances varies from ~12 to

35   ~20%. Actinolitic cores within amphibole grains likely represent reaction between olivine

36   precursor and hydrous melt, as evidenced by their high Cr and Ni contents. Amphibole

37   thermometry and oxybarometry calculations indicate that crystal accumulation occurred over

38   temperatures of 857–1014 °C, at mid-crustal pressures of 312 to 692 MPa and oxygen fugacity

39   between 0.4 and 1.9 log units above the nickel–nickel oxide buffer. Quantification of the

40   major-element compositions of the parent liquids indicates that the Zhazhalong amphibole

41   cumulates crystallized from basaltic to andesitic magmas, probably with a shoshonitic affinity,

42   and with SiO_2 contents of 46.4–66.4 wt%. Appropriate partition coefficients, calculated using a

43   parameterized lattice strain model and an empirical partitioning scheme, were employed to

44   calculate the trace-element compositions of the liquids in equilibrium with amphibole. Our results

45   confirm that Dy/Yb and Dy/Dy* ratios, which decrease with increasing degrees of differentiation,

46   can be used as robust signatures of amphibole fractionation. This work presents a direct snapshot

47   of the process of amphibole fractionation and provides a natural example of the hidden

48   amphibole 'sponge' in arc crust. In particular, this study also suggests that some appinites likely

49   represent amphibole-rich cumulates, which may help to explain the genesis of other unusual but

50   petrologically significant rocks.

51   **Keywords:** amphibole, fractional crystallization, cumulate, magma evolution, trace element

52

53

54   **INTRODUCTION**

55   Arc magmatism at subduction zones represents the sites of production of new continental

56   crust (Rudnick 1995). There is a little dispute that primitive arc magmas are generated by partial

57   melting in the mantle wedge in response to the dehydration of down-going slabs (e.g., Tatsumi

58   1989; Hawkesworth et al. 1993; Ulmer and Trommsdorff 1995; Grove et al. 2002). However, few

59   of these mantle-derived magmas reach the surface without significant modification. Various

60   processes have been proposed to explain the origin of evolved magmas. Remelting of preexisting

61   crust is commonly invoked in the petrogenesis of granitoid plutons (e.g., Chappell and White

62   1992; Clemens and Stevens 2012; Brown 2013), and there is compelling evidence for a genetic

63   link between metasedimentary rocks and strongly peraluminous granites (Chappell and White

64   1992). Crustal melting is efficient where heat is supplied by underplating mafic magmas (e.g.,

65   Petford et al. 2000). Thus, partial melting of the crust is sometimes regarded as a concomitant

66   process in deep-crustal hot zones, where fractional crystallization of mantle-derived basaltic

67   parents, partial melting of the surrounding crust, and hybridization of residual and crustal melts

68   occur simultaneously (Hildreth and Moorbath 1988; Annen et al. 2006).

69   Over the past decade, a growing number of studies have supported fractional crystallization

70   of hydrous basaltic magmas as the dominantly process responsible for the production of

71   intermediate and silicic magmas (e.g., Lee and Bachmann 2014; Jagoutz and Klein 2018).

72   Experimental results suggest that the origin of compositional diversity in magmas can be

73   attributed mainly to fractional crystallization (e.g., Grove and Brown 2018; Müntener and Ulmer

74   2018). Field observations and detailed studies of natural rock suites, such as the well-exposed

75   Kohistan Arc Complex, Pakistan, support the laboratory data (e.g., Jagoutz et al. 2006). Recently,

76   an emerging view has been that magmas within transcrustal magmatic systems are stored as

77   high-crystallinity mushes (e.g., Bachmann and Huber 2016; Cashmann et al. 2017), providing a

78   potential physical mechanism for fractional crystallization in crustal distillation columns (e.g.,

79   Bachmann and Huber 2019). However, this concept is debated, in particular with respect to

80   explaining the relationship between volcanic and plutonic rocks (e.g., Bachmann et al. 2007;

81   Glazner et al. 2015), and the genesis of zoned intrusive suites (e.g., Clemens and Stevens 2012;

82   Coleman et al. 2012; Putirka et al. 2014; Barnes et al. 2016).

83   Research has become increasingly focused on the detailed processes of fractional

84   crystallization during magma evolution. Most arc magmas are enriched in H_2O (Plank et al. 2013)

85   and can stabilize amphibole at pressures corresponding to the middle and lower crust (e.g., Grove

86   et al. 2003; Alonso-Perez et al. 2009). Although amphibole is rarely present as a major mineral in

87   erupted volcanic rocks (Davidson et al. 2007), probably owing to the instability of amphibole at

88   low pressures (Rutherford and Devine 1988), trends of increasing La/Yb and decreasing Dy/Yb

89   with increasing SiO_2 suggest that removal of amphibole is widespread during the evolution of arc

90   magmas (so-called 'cryptic amphibole fractionation'; Davidson et al. 2007). If so, this amphibole

91   'sponge' would accumulate at intermediate crustal depths and may constitute a significant

92   reservoir of H_2O (Davidson et al. 2007). Thus, determining where these hidden amphibole

93   sponges are located, how they form, and how they affect magma differentiation, is critical to

94   better understanding crustal growth and the crustal water reservoir. Studies of derivative magmas

95   may fail to provide convincing evidence concerning this differentiation process, because liquids

96   derived from different processes may have similar chemical compositions (e.g., Müntener and

97   Ulmer 2018). In contrast, crustal cumulates may be more useful in constraining deep magmatic

98   processes (e.g., Chin et al. 2018). Hence, there has been increasing interest in the use of

99   amphibole-rich xenoliths to explore the formation of amphibole-rich cumulates and the role of

100   amphibole fractionation during magma evolution (e.g., Tiepolo and Tribuzio 2008; Tollan et al.

101   2012; Smith 2014; Stamper et al. 2014; Cooper et al. 2016; Klaver et al. 2017; Melekhova et al.

102   2017; Chang and Audétat 2018).

103   Exposed within the Himalayan–Tibetan orogen, the Gangdese arc is an ideal place to assess

104   amphibole fractionation and its influences on the evolution of arc magmas because it includes

105   abundant amphibole-rich mafic intrusions and xenoliths (e.g., Ma et al. 2013; Xu et al. 2015;

106   Meng et al. 2016; Ma, X. et al. 2018; Wang et al. 2019; Xu et al. 2019). We performed a detailed

107   case study of amphibole-rich xenoliths within the Zhazhalong intrusive suite, part of the

108   Gangdese arc. Whole-rock and mineral chemistry were carried out on the xenoliths to explore

109   their petrogenesis and to provide a quantitative assessment of the role of amphibole fractionation

110   during magma evolution.

111

112   **GEOLOGIC SETTING**

113   The Gangdese arc, exposed in the large-scale Himalayan–Tibetan orogen, is a fossil

114   continental arc that was sandwiched between the Indian and Asian plates during continental

115   collision and which extends along strike for more than 1500 km (Chung et al. 2005). To the

116   northwest, the arc connects with the Ladakh and Kohistan arcs (Fig. 1; Ji et al. 2009; Jagoutz

117   2010). The Gangdese arc is subdivided into northern and southern parts, which are bounded by

118   the Luobadui–Milashan Fault. The northern part is located within the central Lhasa subterrane,

119   where most igneous rocks have highly evolved isotopic compositions, whereas the southern part

120   extends along the Eurasian continental margin, where most of the magmatic rocks have less

121   radiogenic isotopic compositions (e.g., Zhu et al. 2011; Hou et al. 2015a). Although the precise

122   time of initial collision between the Indian and Asian continents remains controversial (Ding et al.

123   2017), Triassic to early Tertiary magmatism in the Gangdese arc originated through subduction of

124   the Tethyan Ocean lithosphere along the southern margin of the Lhasa Terrane (Chung et al.

125   2005). A minimum age for initiation of subduction is indicated by ~237 Ma andesites, although

126   the polarity of subduction is debated (e.g., Ji et al. 2009; Zhu et al. 2011). Zircon U–Pb ages show

127   that magmatic activity in the arc occurred between 237 and 10 Ma (e.g., Ji et al. 2009; Zhu et al.

128   2011; Hou et al. 2015a), with this magmatism being represented mainly by the voluminous

129   Gangdese Batholith and coeval volcanic rocks. The magmatism can be divided into four stages,

130   with corresponding peaks of ∼190, ∼90, ∼50, and ∼16 Ma (Zhu et al. 2011; Ji et al. 2014). The

131   most voluminous and intense magmatic event occurred during the early Tertiary (∼50 Ma) (Mo et

132   al. 2008). The Gangdese Batholith comprises gabbro, diorite, granodiorite, monzogranite, and

133   syenogranite (e.g., Ji et al. 2009), along with peraluminous leucogranites (e.g., Ma, L. et al. 2018).

134   Amphibole-rich intrusions and xenoliths are associated primarily with intrusions that pre-date the

135   India–Eurasia collision (e.g., Ma et al. 2013; Xu et al. 2015; Ma, X. et al. 2018; Wang et al. 2019;

136   Xu et al. 2019).

137

138   **SAMPLING AND PETROLOGY**

139   The xenoliths studied here were collected from granites of the Zhazhalong intrusive suite,

140   which is located in the central Gangdese arc (Fig. 1). In hand specimen, the xenoliths are black or

141   dark–brown in color (Fig. S1) and contain abundant amphibole with grain sizes generally

142   between 0.1 and 1 mm (Fig. 2a and b). Amphibole crystals are euhedral or subhedral and

143   commonly display a poikilitic texture, with large oikocrysts containing euhedral to subhedral

144   crystals of Cr-spinel, minor apatite (Fig. 2c), and pyrite. Magnetite rims around Cr-spinel grains

145   are common (Fig. 2c). The groundmass is generally dominated by irregularly shaped quartz and

146   K-feldspar, with minor plagioclase. K-feldspar shows extensive low-temperature alteration.

147   Acicular grains of apatite are also present.

148   The crystallization sequence of the xenoliths can be determined through textural

149   observations. Cr-spinel was the first phase to crystallize, followed by amphibole. Apatite occurs

150   as inclusions in amphibole as well as acicular crystals in the groundmass, suggesting a wide

151   range of crystallization interval. Fine-grained anhedral quartz and K-feldspar in the groundmass

152   likely crystallized from the interstitial liquid. In addition, some amphibole grains have cores of

153   actinolite (Fig. 2d).

154

155   **ANALYTICAL METHODS**

156   Zircon U–Pb dating of the host granites was performed using a Neptune multi-collector inductively

157   coupled plasma–mass spectrometry (ICP–MS) instrument coupled with a Newwave UP213 laser-ablation (LA)

158   system at the Institute of Mineral Resources, Chinese Academy of Geological Sciences, Beijing, China. The

159   operating conditions used during the analyses were a beam diameter of 25 μm, a repetition rate of 10 Hz, and a

160   beam energy of 2.5 J/cm^2. Analyses used the GJ-1 zircon as an internal standard. Detailed operating conditions

161   and analytical procedures followed Hou et al. (2009). Off-line selection, integration of background and

162   analytical signals, time-drift corrections, and quantitative calibrations for the U–Pb data were calculated using

163   the software *ICPMSDataCal* (Liu et al. 2010).

164   Major- and trace-element analyses were performed at the Analytical Laboratory of the Beijing Research

165   Institute of Uranium Geology, Beijing, China. Major-element compositions were determined using X-ray

166   fluorescence spectrometry, for which the analytical uncertainty was better than 1%. Trace-element analyses

167   were performed using ICP–MS, for which the precision was better than 5%.

168   Compositions of minerals within the xenoliths were analyzed using a JEOL JXA 8230 electron probe

8

169   micro-analyzer with a 15 kV accelerating voltage, 20 nA beam current, and 1 μm spot size, at the Key

170   Laboratory of Mineralogy and Metallogeny of the Guangzhou Institute of Geochemistry, Chinese Academy of

171   Sciences (GIG–CAS), Guangzhou, China, and a JEOL JXA 8100 electron microprobe (EMP) with a 15 kV

172   accelerating voltage, 20 nA beam current, and 5 μm spot size, at the Institute of Geology, Chinese Academy of

173   Geological Sciences, Beijing, China. In both cases, ZAF correction routines were employed, and both natural

174   and synthetic standards were used. Trace-element abundances were measured by an ELEMENT XR (Thermo

175   Fisher Scientific) ICP–sector field (SF)–MS instrument coupled with a 193 nm (ArF) Resonetics RESOlution

176   M-50 LA system at the State Key Laboratory of Isotope Geochemistry (SKLaBIG), at GIG–CAS. All LA–ICP–

177   MS spots were located over EMPA spots. Analyses used a spot size of 33 μm, a laser repetition rate of 5 Hz,

178   and a pulse energy of ~4 J cm^{-2}. A smoothing device (The Squid, Laurin Technic) was used to smooth the

179   sample signal. For each analysis, a 20 s gas blank (laser off) and a 30 s sample signal (laser on) were collected

180   and recorded. Measurements were carried out under the E-scan mode. United States Geological Survey (USGS)

181   reference glasses BHVO-2G, BCR-2G, and GSD-1G were employed to construct the calibration line for each

182   element. The oxide molecular yield ($^{238}U^{16}O/^{238}U$ ratio) was less than 0.3%. USGS reference glass TB-1G was

183   determined as an unknown sample, which indicated that most elements are within 10% of the reference values,

184   with an analytical precision (2RSD, relative standard deviations) of better than 12% for most elements

185   (Supplementary Table S1). Details of the experimental procedure and data reduction strategy used are described

186   by Zhang et al. (2019). SiO_2 contents determined by electron microprobe were used as an internal

187   standardization to normalize trace-element abundances.

188

189   **RESULTS**

9

Zircon U–Pb geochronology

LA–ICP–MS U–Pb dating was performed on euhedral and complexly zoned zircons from two host granites, with a total of 50 analyses being obtained. The data and concordia diagrams are given in Supplementary Table S2 and presented in Figure S1, respectively. One sample yielded a weighted mean age of 209.7 ± 2.6 Ma (2σ; n = 15; MSWD = 0.3), and another yielded an age of 208.4 ± 1.8 Ma (2σ; n = 17; MSWD = 1.6). Although we did not find an appropriate method to determine the age of the xenoliths, cross-cutting granitic veins (Fig. S2) indicate that the xenoliths formed before solidification of the host granite, during the early stages of Neotethyan subduction (Ji et al. 2009).

Whole-rock geochemical compositions

Whole-rock chemical compositions of the Zhazhalong xenoliths and host granites are presented in Table 1. The xenoliths have SiO_2 contents varying from 42.41 to 45.95 wt%, with Al_2O_3 abundances from 13.00 to 13.97 wt%, Fe_2O_3 (total) abundances from 9.40 to 10.46 wt%, MgO contents from 9.58 to 11.37 wt%, CaO abundances from 7.52 to 11.90 wt%, and K_2O abundances from 1.75 to 3.86 wt%. The Mg# (atomic Mg/[Mg + Fe_{total}] × 100) ranges from 67 to 69. On chondrite-normalized rare-earth element (REE) plots (Fig. 3), the xenoliths are depleted in heavy REEs (HREEs), enriched in light REEs (LREEs), and have weak negative Eu anomalies. They have near-chondritic or slightly sub-chondritic Zr/Hf ratios (30.2 to 35.8), sub-chondritic Nb/Ta ratios (10.9 to 15.7), Sr/Y ratios (13.0 to 15.9), high Dy/Yb values (1.9 to 2.6), and low Dy/Dy* values (0.5 to 0.6), where Dy/Dy* = $Dy_N/(La_N^{4/13} \times Yb_N^{9/13})$ (Davidson et al. 2013), and Dy_N, La_N, and Yb_N represent chondrite-normalized (Sun and McDonough 1989) values of Dy, La,

10

211 and Yb, respectively.

Mineral major- and trace-element compositions

213 Representative analyses for the major- and trace-element contents of different minerals are

214 given in Tables 2–4; the full list of analyses of amphibole is provided in Supplementary Table S1.

Amphibole

216 Magmatic amphibole in the xenoliths displays a narrow range in SiO_2 (37.92–43.58 wt%)

217 and Al_2O_3 (10.55–14.49 wt%) contents. It is characterized by a limited range in Ti (0.06 to 0.37

218 atoms per formula unit, apfu; per 23 oxygen), Al_{total} (1.49 to 2.57 apfu), and alkali (Na + K; from

219 0.34 to 0.92 apfu) contents, and has Mg# of 62–74. Most of the amphiboles are classified as

220 magnesiohastingsite or pargasite (Leake et al. 1997; Fig. 4). Hereafter, we use the term

221 'amphibole' when referring to magnesiohastingsite or pargasite. On chondrite-normalized REE

222 diagrams (Fig. 3), the amphiboles are enriched in LREEs, depleted in HREEs, and have weak or

223 absent Eu anomalies. Amphibole compositions have a range of Zr/Hf (22.1 to 42.1), Nb/Ta (16.1

224 to 26.0), Sr/Y (12.0 to 20.6), Dy/Yb (1.7 to 3.0), and Dy/Dy* (0.4 to 0.9) ratios.

Actinolite

226 Actinolite commonly occurs as inclusions in amphibole (Fig. 2d). Compared with the

227 composition of amphibole, actinolite contains higher SiO_2 (54.22–56.01 wt%) and MgO (19.55–

228 20.76 wt%) contents, and lower Al_2O_3 (0.34–2.20 wt%), TiO_2 (<0.40 wt%), FeO (7.25–8.64

229 wt%), and Na_2O (0.05–0.22 wt%) contents, with higher Mg# (77 to 84). Actinolite also shows

230 variable Zr/Hf (34.9 to 118.6), and Sr/Y ratios (7.8 to 83.5).

Cr-spinel

232   Cr-Spinel also forms inclusions in amphibole. The dominant spinel composition is high

233   MgO (6.92–10.89 wt%), with variable Cr# (atomic Cr/[Cr + Al] × 100) of 53–58 and Mg# of 27–

234   42.

235

236   **DISCUSSION**

237   **A cumulate origin for the Zhazhalong xenoliths**

238   The occurrence of amphibole-rich xenoliths in subduction-related igneous rocks is widely

239   documented, and they are particularly common in island arcs (e.g., Arculus and Wills 1980;

240   Davidson and Wilson 2011). Several possible explanations have been proposed for the origin of

241   these xenoliths, including phenocryst clusters, entrained fragments of wall rocks or deep

242   basement, and xenoliths of cumulate material (e.g., Tollan et al. 2012). The framework of

243   euhedral amphibole grains in the xenoliths studied here is consistent with an igneous origin.

244   Formation of amphibole-rich lithologies can be attributed to two mechanisms. One possibility is

245   that they formed by nucleation, growth, and settling of amphibole crystals from parental liquids

246   (e.g., Davidson et al. 2007). An alternative is that they developed through a peritectic reaction

247   whereby early crystallized clinopyroxene or olivine reacted with residual or melts injected from

248   elsewhere (e.g., Smith 2014; Humphreys et al. 2019a). Many studies have presented petrographic

249   evidence supporting the formation of amphibole by reaction between melt and clinopyroxene

250   (e.g., Smith 2014; Cooper et al. 2016; Klaver et al. 2017; Melekhova et al. 2017; Stamper et al.

251   2017).   However,   the   following   lines   of   evidence   suggest   that   the   Zhazhalong

252   amphibole-dominated xenoliths formed by direct crystal accumulation: (1) the xenoliths are

12

253   characterized by a framework of idiomorphic amphibole grains (Fig. 2a and b); (2) the mineral–

254   whole-rock Fe–Mg exchange coefficient (Fig. 5a), which is an effective signature of crystal

255   accumulation (Putirka 2016; Barnes et al. 2016), indicates a cumulate origin for the xenoliths; (3)

256   the REE compositions of the xenoliths, which are enriched in LREEs relative to HREEs, are

257   similar to those of the amphibole itself (Fig. 3); (4) the melts that are inferred to have been in

258   equilibrium with amphibole have similar compatible trace-element contents, but significantly

259   higher incompatible trace-element contents, compared with the xenoliths (as discussed in the next

260   section); and (5) the SiO_2 content of the melt in equilibrium with amphibole can be estimated

261   using the amphibole composition alone (Ridolfi et al. 2010; Erdmann et al. 2014; Putirka 2016),

262   with calculations showing that the Zhazhalong amphibole crystallized from basaltic to andesitic

263   magmas (46.4–66.4 wt% SiO_2; Fig. 5b), which contrasts with the whole-rock compositions of the

264   xenoliths (42.41–45.95 wt% SiO_2).

265   Although the Zhazhalong xenoliths are likely to be of cumulate origin, potential

266   reaction-replacement processes prior to amphibole accumulation can also be recognized. Some

267   amphibole grains have a core of actinolite that is surrounded by lower-silica, more aluminous

268   calcic amphibole similar in composition to that of other idiomorphic amphiboles in the xenoliths

269   (Fig. 2d). Actinolite is generally expected to be a product of subsolidus reaction, and overprints

270   earlier amphibole along grain boundaries, cracks, and cleavage planes (Martin 2007). Actinolitic

271   cores surrounded by aluminous, calcic amphibole is the reverse of that expected due to magma

272   crystallization (Martin 2007). A probable explanation is that the core is a pseudomorph after

273   primary pyroxene or olivine (e.g., Compton 1958; Zhang et al. 2015; Humphreys et al. 2019a).

13

274   Thus, the actinolite crystals within the interior of some amphibole grains may represent

275   replacement of olivine due to reaction with hydrous melts, as evidenced by the significantly high

276   contents of Cr and Ni in the cores (Table 3). This interpretation is also consistent with the high

277   Cr and Ni whole-rock contents of the Zhazhalong xenoliths (Table 1).

278

279   **Physical conditions for amphibole accumulation**

280   Studies of plutonic xenoliths have provided important insights into deep-crustal processes,

281   not only in arc magmatic systems (e.g., Arculus and Wills 1980; Tollan et al. 2012; Cooper et al.

282   2016; Melekhova et al. 2017; Stamper et al. 2017; Chin et al. 2018) but also in continental rift

283   settings (e.g., Chin 2018). Here, we use multiple thermodynamic calibrations to place constraints

284   on the formation of the Zhazhalong cumulate lithologies. Calibrations based on a specific mineral

285   assemblage or amphibole–liquid exchange equilibria are not applicable to cumulate rocks

286   because of the lack of appropriate mineral assemblages and knowledge of the composition of

287   parental melts. Amphibole is abundant in the Zhazhalong xenoliths, thus empirical

288   thermobarometric formulas depending on the compositions of individual amphiboles were

289   employed to estimate the conditions of crystal accumulation (Ridolfi et al. 2010; Putirka 2016).

290   Given the test of Erdmann et al. (2014), oxygen fugacity was estimated using the method of

291   Ridolfi et al. (2010); temperatures, and the SiO_2 contents of coexisting liquids, were calculated

292   using the equations of Putirka (2016). Figure 5b–d shows the full range of equilibrium liquid

293   SiO_2 contents, temperatures, pressures, and oxygen fugacities for the Zhazhalong cumulate

294   xenoliths. The modeled temperatures are in the range 857–1034 °C (Fig. 5c), and oxygen fugacity

295   is 0.4 to 1.9 log units above the nickel–nickel oxide buffer (ΔNNO = 0.4–1.9; Fig. 5d). As

296   mentioned above, the calculated equilibrium liquids have SiO_2 contents of 46.4–66.4 wt% (Fig.

297   5b). Application of the Ridolfi et al. (2010) model gives pressures from 312 to 692 MPa (Fig. 5c).

298   However, for low-Si amphibole that crystallizes from mafic to intermediate magmas, the Ridolfi

299   et al. (2010) model overestimates pressure (Erdmann et al. 2014). Thus, the Zhazhalong xenoliths

300   likely formed at mid-crustal depths.

301

302   **Compositions of the equilibrium liquids**

303   Understanding of the compositional relationship between cumulates and their coexisting

304   liquids is derived mainly from experimental studies (e.g., Müntener and Ulmer 2018).

305   Approaches based on natural examples are rare because of the difficulty of predicting liquid

306   compositions based on that of the cumulate. In addition, although the thermodynamic modeling

307   software MELTS has been widely used to track the evolution of mafic–intermediate magmas

308   (Ghiorso and Sack 1995), the algorithms in MELTS cannot easily deal with amphibole

309   fractionation (Ghiorso 1997). Here, we attempt to provide a quantitative assessment of the

310   chemical compositions of the liquids that coexisted with the Zhazhalong cumulates.

311   A series of empirical chemometric equations for calculating the major-element compositions

312   of liquids in equilibrium with amphibole based on an expanded data set of experimental results

313   were proposed by Zhang et al. (2017) and updated by Humphreys et al. (2019b). Using these

314   equations, the melt major-element compositions (i.e., SiO_2, TiO_2, Al_2O_3, FeO_{total}, MgO, CaO, and

315   K_2O as wt%) were obtained (Supplementary Table S1). Based on amphiboles from the

15

316   Zhazhalong cumulate xenoliths, the calculated melts have 48.6–65.7 wt% SiO_2, 0.2–1.5 wt%

317   TiO_2, 15.2–19.1 wt% Al_2O_3, 3.4–11.8 wt% FeO_{total}, 1.2–7.7 wt% MgO, 3.5–9.6 wt% CaO, 0.9–

318   3.3 wt% K_2O, and Mg# of 32–58 (Supplementary Table S1). A comparison of the SiO_2 contents

319   of the melts using the formulation of Putirka (2016) with those using the method of Zhang et al.

320   (2017) shows excellent agreement (Fig. 6a). To assess the reliability of the calculated melt

321   compositions, we performed a test for amphibole–liquid Fe–Mg exchange equilibrium, following

322   the approach of Putirka (2016). The Fe–Mg exchange coefficient K_D(Fe–Mg)$^{amphibole–liquid}$

323   (hereafter K_D)is defined as:

324

$$K_D = \frac{X_{FeOt}^{Amp}/X_{MgO}^{Amp}}{X_{FeOt}^{Liquid}/X_{MgO}^{Liquid}} \quad (1)$$

325

326   where FeOt represents total Fe as FeO. Amphibole–liquid pairs with K_D of 0.28 ± 0.11 (Putirka

327   2016) were regarded to be in chemical equilibrium. As shown in Figure 6b, most amphibole–

328   liquid pairs were in or near Fe–Mg exchange equilibrium. Thus, the Zhazhalong amphibole-rich

329   cumulates likely crystallized from basaltic to andesitic magmas.

330   The most challenging issue in the calculation of trace-element compositions of liquids based

331   on amphibole chemistry is that amphibole/melt partition coefficients can vary significantly under

332   different conditions (Tiepolo et al. 2007), with application of different partition coefficients

333   producing diverse results (e.g., Barnes et al. 2017). Trace-element partitioning between

334   amphibole and liquid is sensitive to temperature, pressure, crystal chemistry, and melt

16

335   composition (Tiepolo et al. 2007), so application of a single set of experimentally determined

336   partition coefficients to natural samples is associated with large uncertainties. Parameterized

337   trace-element-partitioning models may solve this difficulty (Brice 1975; Blundy and Wood 1994;

338   Wood and Blundy 1997; Shimizu et al. 2017; Humphreys et al. 2019). The partitioning behavior

339   of REEs is well understood and can be easily fitted by a lattice strain model (Blundy and Wood

340   1994; Shimizu et al. 2017). According to the model, the partition coefficients of trace elements

341   between amphibole and liquid can be expressed as:

342

$$D_i^{Amp-liquid} = D_0 \exp\left[-\frac{4\pi E N_A}{RT}\left(\frac{r_0}{2}(r_0 - r_i)^2 - \frac{1}{3}(r_0 - r_i)^3\right)\right] \quad (2)$$

343

344   where D_i and D_0 are the theoretical and strain-free amphibole–liquid partition coefficients,

345   respectively; r_0 is the optimum radius of the lattice site; r_i is the ionic radius of element; E is the

346   effective Young's modulus; R is the gas constant (8.3145 J/mol·K); N_A is Avogadro's number;

347   and T is the temperature in Kelvin. The parameters (D_0, r_0, and E) are a function of pressure,

348   temperature, and composition, which Shimizu et al. (2017) quantified through a parameterized

349   model based on amphibole compositions:

350

$$\ln D_0 = -4.21 + \frac{7.27 \times 10^4}{RT} + 1.52X_{Ti}^{Amp} - 0.35X_{Mg}^{Amp} - 1.83X_{Na}^{Amp} - 2.95X_{K}^{Amp} \quad (3)$$

$$r_0 = 1.043 - 0.039X_{Fm}^{Amp-M4} \quad (4)$$

$$E = 337 \quad (5)$$

$$X_{Fm}^{Amp-M4} = X_{Fe^{2+}}^{Amp-M4} + X_{Mn^{2+}}^{Amp-M4} + X_{Mg}^{Amp-M4} \quad (6)$$

17

351

352   where $X_{\text{Ti}}^{\text{Amp}}$, $X_{\text{Mg}}^{\text{Amp}}$, $X_{\text{Na}}^{\text{Amp}}$, and $X_{\text{K}}^{\text{Amp}}$ are the number of cations (per 23 oxygens), and

353    $X_{\text{Fe}^{2+}}^{\text{Amp}-\text{M4}}$, $X_{\text{Mn}^{2+}}^{\text{Amp}-\text{M4}}$, and $X_{\text{Mg}}^{\text{Amp}-\text{M4}}$ are the number of cations on the M4 site. Amphibole cation

354   site occupancies and Fe^{2+} cation numbers were estimated using Putirka (2016).

355   The calculated partition coefficients of REEs and Y for the Zhazhalong amphiboles are given

356   in Supplementary Table S1 and shown in an Onuma diagram (Fig. 7a). Partition coefficients for

357   other trace elements were predicted using the empirical scheme of Humphreys et al. (2019), and

358   only elements with good linear fits (adjusted $R^2 > 0.6$) were utilized. Partition coefficients for La

359   and Dy that were calculated using two independent methods are shown for comparison in Figure

360   7b and c, respectively. Overall, the partition coefficients that were calculated using the

361   Humphreys et al. (2019) model have values that are slightly higher than those calculated using

362   the Shimizu et al. (2017) model. The partition coefficients for REEs and Y using the Shimizu et al.

363   (2017) model and for Rb and Sr based on the Humphreys et al. (2019) scheme were then

364   employed to calculate the trace-element compositions of the liquids from which the Zhazhalong

365   amphiboles crystallized. The compositions of the equilibrium liquids are characterized by

366   enrichment of LREEs over HREEs and an absence of a negative Eu anomaly, comparable with

367   the features observed in the amphiboles, albeit with higher LREE (Fig. 3) and Sr contents

368   (Supplementary Table S1).

369

370   **The role of amphibole fractionation during magma evolution**

371   Our study demonstrates that the role of amphibole-controlled fractionation on the evolving

372   chemical of magmas can be assessed on the basis of an investigation of cumulates. Amphibole in

373   the Zhazhalong cumulate xenoliths is characterized by low SiO_2 and high TiO_2 contents. Thus,

374   precipitation of amphibole can drive derivative melts towards higher SiO_2 and lower TiO_2

375   contents. The wide range of calculated temperatures (857 to 1037 °C; Fig. 5c) can be attributed to

376   multiple factors, such as analytical errors, inherent uncertainties in the thermometric calculations,

377   and crystallization temperatures. However, liquids in equilibrium with amphibole become

378   successively enriched in incompatible elements (e.g., La; Fig. 8a) and depleted in compatible

379   elements (e.g., Dy; Fig. 8b) with decreasing temperature. Thus, the variability in temperatures

380   reflects mainly crystallization and/or post-cumulus overgrowths. Similar differentiation trends are

381   not obvious in plots versus amphibole Mg# (Fig. 8d and e). Amphibole Mg# is correlated

382   positively not only with parental melt composition but also with H_2O content and oxygen

383   fugacity (Fig. 9a; Grove et al. 2003; Krawczynski et al. 2012). In the present study, decoupling

384   between the Mg# of amphibole and temperature probably reflects an increase in oxygen fugacity

385   with cooling (Fig. 9b).

386   The concentrations of compatible trace elements in the equilibrium liquids almost overlap

387   with the whole-rock compositions of the xenoliths (such as Dy; Fig. 8b and e). In contrast, the

388   concentrations of incompatible trace elements in the equilibrium liquids are significantly higher

389   than in the xenoliths (such as La; Fig. 8a and d). This discrepancy may result from post-cumulus

390   compaction and upward expulsion of evolved interstitial liquid that was enriched in incompatible

391   trace elements. This process (i.e., solidification accompanied by compaction) has been

392   recognized in many igneous cumulates (e.g., Meurer and Boudreau 1998). Following the

19

393   approach of Meurer and Boudreau (1998), we estimated the trapped liquid fraction using trace

394   elements (La, Ce, and Dy) whose partitioning behavior is well understood in this study. The

395   results indicate that the weight proportion of trapped liquid varies from 12 to 20%. Although the

396   Zhazhalong amphiboles are characterized by very high contents of some elements, such as Sr,

397   there is no appreciable decrease in the Sr content of equilibrium liquid with decreasing

398   temperature (Fig. 8c). Consequently, precipitation of amphibole had a negligible effect on the Sr

399   composition of the residual liquid.

400   Trends of decreasing Dy/Yb and Dy/Dy* ratios with increasing SiO_2 are regarded as key

401   evidence for amphibole fractionation during magma evolution (Davidson et al. 2007, 2013). To

402   further test this hypothesis, we investigated Dy/Yb and Dy/Dy* variations using the compositions

403   of the cumulates studied here (Fig. 10). The modeled changes in the Dy/Yb and Dy/Dy* ratios of

404   derivative liquids and cumulates with increasing degrees of differentiation, assuming that

405   amphibole was a major fractionating phase, are shown in Figure 10b. The results show apparently

406   decreasing Dy/Yb and Dy/Dy* ratios in the liquids with progressive removal of amphibole.

407   Therefore, our results confirm that Dy/Yb and Dy/Dy* ratios are robust geochemical fingerprints

408   of amphibole crystallization during magma evolution.

409   It is also noteworthy that the amphiboles in this study have unusually high Sr (511 ± 65

410   ppm), Ba (944 ± 261 ppm), and LREE contents. The Sr contents of the equilibrium liquids range

411   from 885 to 1402 ppm, based on the partitioning scheme of Humphreys et al. (2019). Thus the

412   parental melts of the Zhazhalong amphiboles were enriched in Sr, Ba, and LREEs

413   (Supplementary Table S1). These geochemical features have been observed in some island arc

414   magmatic rocks (e.g., Sadofsky et al. 2008), which has generally been interpreted to reflect the

415   incorporation of marine sediments into the magma sources (e.g., Othman et al. 1989; Plank and

416   Langmuir 1993). The high contents of large-ion lithophile elements and LREEs, together with

417   plenty of interstitial K-feldspars in the matrix of the xenoliths, suggest that the parent liquids

418   were shoshonitic, which is a compositional series within island arc magma systems (e.g., Stern et

419   al. 1988; Bloomer et al. 1989) or post-collision magmatic settings (e.g., Turner et al. 1996). Only

420   a small amount of the equilibrium melts is inferred to have been shoshonitic, with most belonging

421   to the high K calc-alkaline series (Fig. S3), although the reason for this is unclear. In addition, the

422   Zhazhalong amphibole-rich xenoliths have petrological similarities to appinite, which shows

423   genetic relationships with some particular rock suites, such as high Ba–Sr granites and

424   sanukitoids (e.g., Murphy 2013; Tiepolo and Tribuzio 2008). Our detailed study suggests that, at

425   least in some cases, appinite suites could represent amphibole-rich cumulates derived from

426   water-rich magmas.

427

428   **IMPLICATIONS**

429   The Zhazhalong xenoliths provide a rare example of fragments of arc cumulates in which

430   the crystal framework consists mostly of amphibole. Several independent lines of evidence,

431   including textural characteristics, Fe–Mg exchange coefficients, trace-element signatures, and

432   equilibrium liquid compositions, indicate that the Zhazhalong xenoliths represent fragments of

433   amphibole-rich cumulates formed by crystal accumulation, in which trapped liquid fractions were

434   ~12–20 %. Actinolitic cores within amphibole grains represent reaction products of primary

435   olivine with hydrous melt. Thermometry and oxybarometry based on amphibole compositions

436   indicate that the temperatures of crystal accumulation ranged from 857 to 1014 °C, pressures

437   from 312 to 692 MPa, and oxygen fugacities from 0.4 to 1.9 ΔNNO. The xenoliths likely formed

438   at mid-crustal depths. The major- and trace-element compositions of the parent melts were also

439   quantified. The results show that the Zhazhalong amphiboles crystallized from basaltic to

440   andesitic (probably shoshonitic) magmas with SiO_2 contents of 46.4–66.4 wt%. The equilibrium

441   liquids were also enriched in LREEs and Sr. The previous proposal that decreasing Dy/Yb and

442   Dy/Dy* ratios with increasing differentiation can be used as a signature of amphibole

443   fractionation (Davidson et al. 2007, 2013) is supported by the investigation of cumulate xenoliths

444   in the present study.

445   Our work permits a better understanding of the role of amphibole fractionation during

446   magma evolution. Although the importance of amphibole precipitation has been inferred through

447   distinctive geochemical fingerprints of derivative products, this study provides a direct snapshot

448   of this differentiation process. With progressive accumulation, an amphibole-rich sponge will

449   form in arc crust, which is fundamental to interpreting a wide range of issues in petrology (e.g.,

450   Davidson et al. 2007; Edmonds et al. 2019; Sparks et al. 2019) and perhaps for the genesis of

451   ore-forming magmas (e.g., Hou et al. 2015b, 2017). In particular, the studied amphibole-rich

452   xenoliths have petrological similarities to appinite, suggesting that some appinites may represent

453   amphibole-rich cumulates. This has important implications for understanding the genesis of some

454   unusual but petrologically significant rocks, such as high Ba–Sr granites and sanukitoids

455   (Murphy 2013).

456

ACKNOWLEDGMENTS

466

REFERENCES CITED

468   Alonso-Perez, R., Müntener, O., and Ulmer, P. (2009) Igneous garnet and amphibole fractionation in the roots

469   of island arcs: Experimental constraints on andesitic liquids. Contributions to Mineralogy and Petrology,

470   157, 541–558.

471   Annen C., Blundy J.D., and Sparks R.S.J. (2006) The genesis of intermediate and silicic magmas in deep

472   crustal hot zones. Journal of Petrology, 47, 505–539.

473   Arculus, R.J., and Wills, K.J.A. (1980) The petrology of plutonic blocks and Inclusions from the Lesser

474   Antilles Island Arc. Journal of Petrology, 21, 743–799.

475   Bachmann, O., and Huber, C. (2016) Silicic magma reservoirs in the Earth's crust. American Mineralogist, 101,

476   2377–2404.

477   Bachmann, O., and Huber, C. (2019) The inner workings of crustal distillation columns; the physical

478   mechanisms and rates controlling phase separation in silicic magma reservoirs. Journal of Petrology, 60,

479   3–18.

480   Bachmann, O., Miller, C.F., and de Silva, S.L. (2007) The volcanic-plutonic connection as a stage for

481   understanding crustal magmatism. Journal of Volcanology and Geothermal Research, 167, 1–23.

482   Barnes, C.G., Coint, N., and Yoshinobu, A. (2016) Crystal accumulation in a tilted arc batholith. American

483   Mineralogist, 101, 1719–1734.

484   Barnes, C.G., Berry, R., Barnes, M.A., and Ernst, W.G. (2017) Trace element zoning in hornblende: Tracking

485   and modeling the crystallization of a calc-alkaline arc pluton. American Mineralogist, 102, 2390–2405.

486   Bloomer, S.H., Stern, R.J., Fisk, E., and Geschwind, C.H. (1989) Shoshonitic volcanism in the Northern

487   Mariana Arc: 1. Mineralogic and major and trace element characteristics. Journal of Geophysical Research:

488   Solid Earth, 94, 4469–4496.

489   Blundy, J., and Wood, B. (1994) Prediction of crystal-melt partition coefficients from elastic moduli. Nature,

490   372, 452–454.

491   Brice, J.C. (1975) Some thermodynamic aspects of the growth of strained crystals. Journal of Crystal Growth,

492   28, 249–253.

493   Brown, M. (2013) Granite: From genesis to emplacement. GSA Bulletin 125, 1079–1113.

494   Cashman, K.V., Sparks, R.S.J., and Blundy, J.D. (2017) Vertically extensive and unstable magmatic systems: A

495   unified view of igneous processes. Science, 355, eaag3055.

496   Chang, J., and Audétat, A. (2018) Petrogenesis and metal content of hornblende-rich xenoliths from two

497   Laramide-age magma systems in southwestern USA: insights into the metal budget of arc magmas.

498   Journal of Petrology, 59, 1869–1898.

499   Chappell, B.W., and White, A.J.R. (1992) I- and S-type granites in the Lachlan fold belt. Transactions of the

500   Royal Society of Edinburgh, Earth Science, 83, 1–26.

501   Chin, E.J. (2018) Deep crustal cumulates reflect patterns of continental rift volcanism beneath Tanzania.

502   Contributions to Mineralogy and Petrology, 173, 85.

503   Chin, E.J., Shimizu, K., Bybee, G.M., and Erdman, M.E. (2018) On the development of the calc-alkaline and

504   tholeiitic magma series: A deep crustal cumulate perspective. Earth and Planetary Science Letters, 482,

505   277–287.

506   Chung, S.L., Chu, M.F., Zhang, Y., Xie, Y., Lo, C.H., and Lee, T.Y. (2005) Tibetan tectonic evolution inferred

507   from spatial and temporal variations in post-collisional magmatism. Earth-Science Reviews, 68, 173–196.

508   Clemens, J.D., and Stevens, G. (2012) What controls chemical variation in granitic magmas? Lithos, 134, 317–

509   329.

510   Coleman, D.S., Bartley, J.M., Glazner, A.F., and Pardue, M.J. (2012) Is chemical zonation in plutonic rocks

511   driven by changes in source magma composition or shallow-crustal differentiation? Geosphere, 8, 1568–

512   1587.

513   Compton, R.R. (1958) Significance of amphibole paragenesis in the Bidwell Bar region, California. American

514   Mineralogist, 43, 890–907.

515   Cooper, G.F., Davidson, J.P., and Blundy, J.D. (2016) Plutonic xenoliths from Martinique, Lesser Antilles:

516   evidence for open system processes and reactive melt flow in island arc crust. Contributions to Mineralogy

517   and Petrology, 171, 87.

518   Davidson, J., and Wilson, M. (2011) Differentiation and source processes at Mt Pelee and the Quill; active

519   volcanoes in the Lesser Antilles Arc. Journal of Petrology, 52, 1493–1531.

520   Davidson, J., Turner, S., Handley, H., Macpherson, C., and Dosseto, A. (2007) Amphibole "sponge" in arc crust?

521   Geology, 35, 787–790.

522   Davidson, J., Turner, S., and Plank, T. (2013) Dy/Dy*: variations arising from mantle sources and petrogenetic

523   processes. Journal of Petrology, 54, 525–537.

524   Ding, L., Maksatbek, S., Cai, F., Wang, H., Song, P., Ji, W., Xu, Q., Zhang, L., and Upendra, B. (2017)

525   Processes of initial collision and suturing between India and Asia. Science China Earth Sciences, 60, 635–

526   651.

527   Edmonds, M., Cashman, K.V., Holness, M., and Jackson, M., (2019) Architecture and dynamics of magma

528   reservoirs. Philosophical Transactions of the Royal Society of London A: Mathematical, Physical and

529   Engineering Sciences, 377, 20180298.

530   Erdmann, S., Martel, C., Pichavant, M., and Kushnir, A. (2014) Amphibole as an archivist of magmatic

531   crystallization conditions: problems, potential, and implications for inferring magma storage prior to the

532   paroxysmal 2010 eruption of Mount Merapi, Indonesia. Contributions to Mineralogy and Petrology, 167,

533   1016.

534   Ghiorso, M.S. (1997) Thermodynamic models of igneous processes. Annual Review of Earth and Planetary

535   Sciences, 25, 221–241.

536   Ghiorso, M.S., and Sack, R.O. (1995) Chemical mass-transfer in magmatic processes. 4. A revised and

537   internally consistent thermodynamic model for the interpolation and extrapolation of liquid-solid

538   equilibria in magmatic systems at elevated temperatures and pressures. Contributions to Mineralogy and

539   Petrology, 119, 197–212.

26

540   Glazner, A., Coleman, D., and Mills, R. (2015) The Volcanic-Plutonic Connection, 1–22. Springer, Berlin.

541   Grove, T.L., and Brown, S.M. (2018) Magmatic processes leading to compositional diversity in igneous rocks:

542   Bowen (1928) revisited. American Journal of Science, 318, 1–28.

543   Grove, T.L., Parman, S.W., Bowring, S.A., Price, R.C., and Baker, M.B. (2002) The role of an H_2O-rich fluid

544   component in the generation of primitive basaltic andesites and andesites from the Mt. Shasta region, N

545   California. Contributions to Mineralogy and Petrology, 142, 375–396.

546   Grove, T.L., Elkins-Tanton, L.T., Parman, S.W., Chaterjee, N., Müntener, O. and Gaetani, G.A. (2003)

547   Fractional crystallization and mantle-melting controls on calc-alkaline differentiation trends. Contributions

548   to Mineralogy and Petrology, 145, 515–533.

549   Hawkesworth C.J., Gallagher K., Hergt J.M. and McDermott F. (1993) Mantle and slab contributions in arc

550   magmas. Annual Review of Earth and Planetary Sciences, 21, 175–204.

551   Hildreth, W., and Moorbath, S. (1988) Crustal contributions to arc magmatism in the Andes of Central Chile.

552   Contributions to Mineralogy and Petrology, 98, 455–489.

553   Humphreys, M.C.S., Zhang, J., Cooper, G.F., Macpherson, C.G., and Ottley, C.J. (2019a) Identifying the

554   ingredients of hydrous arc magmas: insights from Mt Lamington, Papua New Guinea. Philosophical

555   Transactions of the Royal Society A, 377, 20180018.

556   Humphreys, M.C., Cooper, G.F., Zhang, J., Loewen, M., Kent, A.J., Macpherson, C.G., and Davidson, J.P.

557   (2019b) Unravelling the complexity of magma plumbing at Mount St. Helens: a new trace element

558   partitioning scheme for amphibole. Contributions to Mineralogy and Petrology, 174, 9.

559   Hou, K.J., Li, Y.H., and Tian, Y.Y. (2009) In situ U–Pb zircon dating using Laser Ablation Multi Ion

560   Counting-ICP-MS. Mineral Deposits, 28, 481–492(in Chinese with English abstract).

561   Hou, Z., Li, Q., Gao, Y., Lu, Y., Yang, Z., Wang, R., and Shen, Z. (2015a) Lower-Crustal magmatic

562   hornblendite in North China Craton: insight into the genesis of porphyry Cu deposits. Economic Geology,

563   110, 1879–1904.

564   Hou, Z., Duan, L., Lu, Y., Zheng, Y., Zhu, D., Yang, Z., Yang, Z., Wang, B., Pei, Y., Zhao, Z., and McCuaig, C.

565   (2015b) Lithospheric architecture of the Lhasa terrane and its control on ore deposits in the

566   Himalayan-Tibetan orogen. Economic Geology, 110, 1541–1575.

567   Hou, Z., Zhou, Y., Wang, R., Zheng, Y., He, W., Zhao, M., Evans, N. J., Weinberg, R. F. (2017). Recycling of

568   metal-fertilized lower continental crust: Origin of non-arc Au-rich porphyry deposits at cratonic edges.

569   Geology, 45, 563–566.

570   Jagoutz, O.E. (2010) Construction of the granitoid crust of an island arc. Part II: a quantitative petrogenetic

571   model. Contributions to Mineralogy and Petrology, 160, 359–381.

572   Jagoutz, O., and Klein, B. (2018) On the importance of crystallization-differentiation for the generation of

573   SiO_2-rich melts and the compositional build-up of arc (and continental) crust. American Journal of Science,

574   318, 29–63.

575   Jagoutz, O., Müntener, O., Burg, J.-P., Ulmer, P. and Jagoutz, E. (2006) Lower continental crust formation

576   through focused flow in km-scale melt conduits: The zoned ultramafic bodies of the Chilas Complex in

577   the Kohistan arc (NW Pakistan). Earth and Planetary Science Letters, 320, 320–342.

578   Ji, W.-Q., Wu, F.-Y., Chung, S.-L., Li, J.-X., and Liu, C.-Z. (2009) Zircon U–Pb geochronology and Hf isotopic

579   constraints on petrogenesis of the Gangdese batholith, southern Tibet. Chemical Geology, 262, 229–245.

580   Ji, W.-Q., Wu, F.-Y., Chung, S.-L., and Liu, C.-Z. (2014) The Gangdese magmatic constraints on a latest

581   Cretaceous lithospheric delamination of the Lhasa terrane, southern Tibet. Lithos, 210, 168–180.

582   Klaver, M., Matveev, S., Berndt, J., Lissenberg, C.J., and Vroon, P.Z. (2017) A mineral and cumulate

583   perspective to magma differentiation at Nisyros volcano, Aegean arc. Contributions to Mineralogy and

584   Petrology, 172, 95.

585   Krawczynski, M.J., Grove, T.L., and Behrens, H. (2012) Amphibole stability in primitive arc magmas: effects

586   of temperature, H_2O content, and oxygen fugacity. Contributions to Mineralogy and Petrology, 164, 317–

587   339.

588   Lee, C.T.A., and Bachmann, O. (2014) How important is the role of crystal fractionation in making

589   intermediate magmas? Insights from Zr and P systematics. Earth and Planetary Science Letters, 393, 266–

590   274.

591   Liu, Y., Gao, S., Hu, Z., Gao, C., Zong, K., and Wang, D. (2010) Continental and oceanic crust

592   recycling-induced melt-peridotite interactions in the Trans-North China Orogen: U–Pb dating, Hf isotopes

593   and trace elements in zircons of mantle xenoliths. Journal of Petrology, 51, 537–571.

594   Ma, L., Wang, Q., Li, Z.-X., Wyman, D.A., Jiang, Z.-Q., Yang, J.-H., Gou, G.-N., and Guo, H.-F. (2013) Early

595   late Cretaceous (ca. 93 Ma) norites and hornblendites in the Milin area eastern Gangdese:

596   Lithosphere-asthenosphere interaction during slab roll-back and an insight into early late Cretaceous (ca.

597   100-80 Ma) magmatic 'flare-up' in southern Lhasa (Tibet). Lithos, 172, 17–30.

598   Ma, L., Wang, Q., Kerr, A.C., Yang, J.-H., Xia, X.-P., Quan, O., Yang, Z.-Y., and Sun, P. (2018) Paleocene (c.

599   62 Ma) Leucogranites in Southern Lhasa, Tibet: products of syn-collisional crustal anatexis during slab

600   roll-back? Journal of Petrology, 58, 2089–2114.

601   Ma, X., Meert, J. G., Xu, Z., and Yi, Z. (2018) Late Triassic intra-oceanic arc system within Neotethys:

602   Evidence from cumulate appinite in the Gangdese belt, southern Tibet. Lithosphere, 10, 545–565.

29

603   Martin, R.F. (2007) Amphiboles in the igneous environment. Reviews in Mineralogy and Geochemistry, 67,

604   323–358.

605   Melekhova, E., Blundy, J., Martin, R., Arculus, R., and Pichavant, M. (2017) Petrological and experimental

606   evidence for differentiation of water-rich magmas beneath St. Kitts, Lesser Antilles. Contributions to

607   Mineralogy and Petrology, 172, 98.

608   Meng, Y., Xu, Z., Santosh, M., Ma, X., Chen, X., Guo, G., and Liu, F. (2016) Late Triassic crustal growth in

609   southern Tibet: evidence from the Gangdese magmatic belt. Gondwana Research, 37, 449–464.

610   Meurer, W.P., and Boudreau, A.E. (1998) Compaction of igneous cumulates Part I: Geochemical consequences

611   for cumulates and liquid fractionation trends. The Journal of Geology, 106, 281–292.

612   Mo, X., Niu, Y., Dong, G., Zhao, Z., Hou, Z., Zhou, S., and Ke, S. (2008) Contribution of syncollisional felsic

613   magmatism to continental crust growth: a case study of the Paleogene Linzizong volcanic succession in

614   southern Tibet. Chemical Geology, 250, 49–67.

615   Murphy, J.B. (2013) Appinite suites: a record of the role of water in the genesis, transport, emplacement and

616   crystallization of magma. Earth-Science Reviews, 119, 35–59.

617   Müntener, O., and Ulmer, P. (2018) Arc crust formation and differentiation constrained by experimental

618   petrology. American Journal of Science, 318, 64–89.

619   O'Neill, H.S.C., and Pownceby, M.I. (1993) Thermodynamic data from redox reactions at high temperatures. I.

620   An experimental and theoretical assessment of the electrochemical method using stabilized zirconia

621   electrolytes, with revised values for the Fe-"FeO", Co-CoO, Ni-NiO and Cu-Cu_2O oxygen buffers, and

622   new data for the W-WO2 buffer. Contributions to Mineralogy and Petrology, 114, 296–314.

623   Othman, D.B., White, W.M., and Patchett, J. (1989) The geochemistry of marine sediments, island arc magma

624   genesis, and crust-mantle recycling. Earth and Planetary Science Letters, 94, 1–21.

625   Petford, N., Cruden, A.R., McCaffrey, K.J.W., and Vigneresse, J.L. (2000) Granite magma formation, transport

626   and emplacement in the Earth's crust. Nature, 408, 669–673.

627   Plank, T., and Langmuir, C.H. (1993) Tracing trace elements from sediment input to volcanic output at

628   subduction zones. Nature, 362, 739–743.

629   Plank, T., Kelley, K.A., Zimmer, M.M., Hauri, E.H., and Wallace, P.J. (2013) Why do mafic arc magmas

630   contain ~4 wt% water on average? Earth and Planetary Science Letters, 364, 168–179.

631   Putirka, K.D. (2016) Amphibole thermometers and barometers for igneous systems and some implications for

632   eruption mechanisms of felsic magmas at arc volcanoes. American Mineralogist, 101, 841–858.

633   Putirka, K.D., Canchola, J., Rash, J., Smith, O., Torrez, G., Paterson, S.R., and Ducea, M.N. (2014) Pluton

634   assembly and the genesis of granitic magmas: Insights from the GIC pluton in cross section, Sierra

635   Nevada Batholith, California. American Mineralogist, 99, 1284–1303.

636   Ridolfi, F., Renzulli, A., and Puerini, M. (2010) Stability and chemical equilibrium of amphibole in

637   calc-alkaline magmas: an overview, new thermobarometric formulations and application to

638   subduction-related volcanoes. Contributions to Mineralogy and Petrology, 160, 45–66.

639   Rudnick, R.L. (1995) Making continental crust. Nature, 378, 571–578.

640   Rutherford, M.J., and Devine, J.D. (1988) The May 18, 1980, eruption of Mount St. Helens: 3. Stability and

641   chemistry of amphibole in the magma chamber. Journal of Geophysical Research: Solid Earth, 93, 11949–

642   11959.

643   Sadofsky, S.J., Portnyagin, M., Hoernle, K., and van den Bogaard, P. (2008) Subduction cycling of volatiles

644   and trace elements through the Central American volcanic arc: evidence from melt inclusions.

645   Contributions to Mineralogy and Petrology, 155, 433–456.

646   Shannon, R.D. (1976) Revised effective ionic-radii and systematic studies of interatomic distances in halides

647   and chalcogenides. Acta Crystallographica, A32, 751–767.

648   Shimizu, K., Liang, Y., Sun, C., Jackson, C.R., and Saal, A.E. (2017) Parameterized lattice strain models for

649   REE partitioning between amphibole and silicate melt. American Mineralogist, 102, 2254–2267.

650   Smith, D.J. (2014) Clinopyroxene precursors to amphibole sponge in arc crust. Nature Communications, 5,

651   4329.

652   Sparks, R.S.J., Annen, C., Blundy, J.D., Cashman, K.V., Rust, A.C., and Jackson, M.D. (2019) Formation and

653   dynamics of magma reservoirs. Philosophical Transactions of the Royal Society of London A:

654   Mathematical, Physical and Engineering Sciences, 377, 20180019.

655   Stamper, C., Blundy, J., Arculus, R., and Melekhova, E. (2014) Petrology of plutonic xenoliths and volcanic

656   rocks from Grenada, Lesser Antilles. Journal of Petrology, 55, 1353–1387.

657   Stern, R.J., Bloomer, S.H., Lin, P.N., Ito, E., and Morris, J. (1988) Shoshonitic magmas in nascent arcs: New

658   evidence from submarine volcanoes in the northern Marianas. Geology, 16(5), 426–430.

659   Tatsumi, Y. (1989) Migration of fluid phases and genesis of basalt magmas in subduction zones. Journal of

660   Geophysical Research: Solid Earth, 94, 4697–4707.

661   Tiepolo, M., and Tribuzio, R. (2008) Petrology and U–Pb zircon geochronology of amphibole-rich cumulates

662   with sanukitic affinity from Husky Ridge (Northern Victoria Land, Antarctica): insights into the role of

663   amphibole in the petrogenesis of subduction-related magmas. Journal of Petrology, 49, 937–970.

664   Tiepolo, M., Oberti, R., Zanetti, A., Vannucci, R., and Foley, S.F. (2007) Trace element partitioning between

665   amphibole and silicate melt. Reviews in Mineralogy and Geochemistry, 67, 417–452.

666   Tollan, P.M.E., Bindeman, I., and Blundy, J.D. (2012) Cumulate xenoliths from St. Vincent, Lesser Antilles

667   island arc: a window into upper crustal differentiation of mantle-derived basalts. Contributions to

668   Mineralogy and Petrology, 163, 189–208.

669   Turner, S., Arnaud, N., Liu, J., Rogers, N., Hawkesworth, C., Harris, N., Kelley, S., van Calsteren, P., and Deng,

670   W. (1996) Post-collision, shoshonitic volcanism on the Tibetan Plateau: Implications for convective

671   thinning of the lithosphere and the source of Ocean Island Basalts. Journal of Petrology, 37, 45–71.

672   Ulmer, P., and Trommsdorff, V. (1995) Serpentine stability to mantle depths and subduction-related magmatism.

673   Science, 268, 858–861.

674   Wang, J., Wang, Q., Dan, W., Yang, J.-H., Yang, Z.-Y., Sun, P., Qi, Y., and Hu, W.-L. (2019) The role of

675   clinopyroxene in amphibole fractionation of arc magmas: Evidence from mafic intrusive rocks within the

676   Gangdese arc, southern Tibet. Lithos, 338, 174–188.

677   Wood, B.J., and Blundy, J.D. (1997) A predictive model for rare earth element partitioning between

678   clinopyroxene and anhydrous silicate melt. Contributions to Mineralogy and Petrology, 129, 166–181.

679   Xu, W.-C., Zhang, H.-F., Luo, B.-J., Guo, L., and Yang, H. (2015) Adakite-like geochemical signature produced

680   by amphibole-dominated fractionation of arc magmas: an example from the Late Cretaceous magmatism

681   in Gangdese belt, south Tibet. Lithos, 232, 197–210.

682   Xu, W., Zhu, D.-C., Wang, Q., Weinberg, R.F., Wang, R., Li, S.-M., Zhang, L.-L., and Zhao, Z.-D. (2019)

683   Constructing the Early Mesozoic Gangdese crust in southern Tibet by hornblende-dominated magmatic

684   differentiation. Journal of Petrology, 60, 515–552.

685   Zhang, L., Ren, Z.-Y., Xia, X.-P., Yang, Q., Hong, L.-B., and Wu, D. (2019) In situ determination of trace

686   elements in melt inclusions using laser ablation inductively coupled plasma sector field mass spectrometry.

33

687   Rapid Communications in Mass Spectrometry, 33, 361–370.

688   Zhang, J., Davidson, J.P., Humphreys, M.C.S., Macpherson, C.G., and Neill, I. (2015) Magmatic enclaves and

689   andesitic lavas from Mt. Lamington, Papua New Guinea: implications for recycling of earlier-fractionated

690   minerals through magma recharge. Journal of Petrology, 56, 2223–2256.

691   Zhang, J., Humphreys, M.C.S., Cooper, G.F., Davidson, J.P., and Macpherson, C.G. (2017) Magma mush

692   chemistry at subduction zones, revealed by new melt major element inversion from calcic amphiboles.

693   American Mineralogist, 102, 1353–1367.

694   Zhu, D.-C., Zhao, Z.-D., Niu, Y., Mo, X.-X., Chung, S.-L., Hou, Z.-Q., Wang, L.-Q., and Wu, F.-Y., 2011. The

695   Lhasa Terrane: record of a microcontinent and its histories of drift and growth. Earth and Planetary

696   Science Letters, 301, 241–255.

697

698   **FIGURE CAPTIONS**

699   **FIGURE 1.** Geologic map of the Zhazhalong intrusive suite showing the sampling location of the

700   amphibole-rich xenoliths. The inset map shows the location of the Gangdese arc and the neighboring Ladakh

701   and Kohistan arcs. The red star in the inset map marks the location of the study area.

702   **FIGURE 2.** Photomicrographs of the xenoliths. (a)–(b) Framework composed of idiomorphic amphibole,

703   anhedral K-feldspar, quartz, and plagioclase; (c) poikilitic amphibole crystal containing a large oikocryst of

704   euhedral Cr-spinel; (d) actinolitic core within calcic amphibole. (a), (c), and (d) are in plane-polarized light; (b)

705   and the inset image in (c) are BSE (back-scattered electron microscopy) images.

706   **FIGURE 3.** Chondrite-normalized (Sun and McDonough 1989) REE patterns for amphibole, whole-rock

707   xenoliths, and liquids in equilibrium with amphibole, with the latter calculated using the Shimizu et al. (2017)

708   partitioning model.

709   **FIGURE 4.** (a) Amphibole compositions. (b) Actinolite compositions. Amphibole cation site occupancies

710   were estimated using Putirka (2016). Classification and nomenclature follow Leake et al. (1997).

711   **FIGURE 5.** (a) Tests of amphibole–liquid Fe–Mg exchange equilibrium. K_D values in the range 0.28 ±

712   0.11 (Putirka 2016) are regarded to be in chemical equilibrium. (b) Relationship between Al_{total} in amphibole

713   and the predicted SiO_2 content of coexisting liquid. The range of compositions of the xenoliths is shown by the

714   horizontal gray bar. (c) and (d) Calculated temperature, pressure, and oxygen fugacity based on amphibole

715   compositions. Oxygen fugacity and pressure were calculated using the method of Ridolfi et al. (2010). The

716   pressure estimates should be treated with caution. Temperatures and the SiO_2 contents of coexisting liquids

717   were calculated using equations 5 and 10 of Putirka (2016), respectively. The calibration of the nickel–nickel

718   oxide (NNO) buffer is taken from O'Neill and Pownceby (1993).

719   **FIGURE 6.** (a) Comparison of predicted liquid SiO_2 contents using the equations of Putirka (2016) and

720   Zhang et al. (2017). (b) Tests of amphibole–liquid Fe–Mg exchange equilibrium. Xenolith–amphibole pairs are

721   also shown.

722   **FIGURE 7.** (a) Onuma diagram for REE and Y partition coefficients as a function of cation radius. Data

723   marked by circles were calculated using the model of Shimizu et al. (2017). The blue lines are the best-fit

724   parabola to the trivalent REEs and Y using the equation of the lattice strain model (Brice 1975; Blundy and

725   Wood 1994; Wood and Blundy 1997). The lattice strain parameters D_0, r_0, and E were obtained using the

726   mineral composition model of Shimizu et al. (2017). Ionic radii are from Shannon (1976). (b) Comparison of

727   predicted D_{La} using the models of Humphreys et al. (2019) and Shimizu et al. (2017). (c) Comparison of

728   predicted D_{Dy} using the models of Humphreys et al. (2019) and Shimizu et al. (2017).

35

729   **FIGURE 8.** (a)–(c) Calculated La, Dy, and Sr concentrations of the equilibrium liquid as a function of

730   temperature. (d)–(f) Calculated La, Dy, and Sr concentrations of the equilibrium liquid as a function of the Mg#

731   of amphibole.

732   **FIGURE 9.** (a) Mg# of amphibole as a function of oxygen fugacity. Oxygen fugacity was constrained

733   using the method of Ridolfi et al. (2010). (b) Temperature versus oxygen fugacity. Temperatures were

734   calculated by using equation 5 of Putirka (2016).

735   **FIGURE 10.** (a) Variation in Dy/Dy* of the equilibrium liquid as a function of temperature. (b)

736   Quantitative assessment of Dy/Yb and Dy/Dy* with amphibole fractionation, using Rayleigh fractionation and

737   our calculated partition coefficients. The calculations assume the average composition of liquids in equilibrium

738   with amphiboles that have temperatures of >1000 °C as an initial composition, where $Dy_N/Yb_N = 1.25$ and

739   Dy/Dy* = 0.24. The average partition coefficients were $D_{La} = 0.1$, $D_{Dy} = 1.2$, and $D_{Yb} = 0.91$. *F* represents melt

740   fraction.

741

742

743

744

745

746

TABLE 1. Bulk-rock major- and trace-element compositions of the Zhazhalong xenoliths and host granites

Sample:	HR2013-2	HR2013-3	HR2013-4	HR2013-5	HR2013-7	HR2013-8	HR2013-10	HR2013-11
Latitude, °N	30.0938	30.0938	30.0938	30.0938	30.0938	30.0938	30.0938	30.0938
Longitude, °E	88.8642	88.8642	88.8642	88.8642	88.8642	88.8642	88.8642	88.8642
Lithology	Granite	Granite	Granite	Granite	Xenolith	Xenolith	Xenolith	Xenolith

36

Major oxides(wt%)

SiO_2	70.12	74.15	70.96	72.14	45.95	42.41	44.96	45.93
TiO_2	0.24	0.16	0.25	0.21	1.12	1.27	1.18	1.19
Al_2O_3	13.01	12.06	12.70	12.95	13.59	13.00	13.70	13.97
TFe_2O_3	2.17	1.46	2.30	1.37	9.77	10.46	9.40	9.58
MnO	0.21	0.32	0.24	0.16	0.48	0.42	0.41	0.49
MgO	1.01	1.00	1.07	0.93	10.97	11.37	9.58	10.28
CaO	1.76	1.21	1.65	1.47	7.52	11.90	10.40	7.86
Na_2O	0.19	0.11	0.14	0.18	0.59	0.63	0.60	0.45
K_2O	6.65	5.54	6.00	6.69	3.82	1.75	3.33	3.86
P_2O_5	0.08	0.05	0.08	0.07	0.49	0.59	0.45	0.52
LOI	4.54	3.83	4.58	3.73	5.15	5.62	5.44	5.36
Total	99.97	99.90	99.97	99.90	99.45	99.42	99.45	99.49

Trace elements (ppm)

Rb	337	342	328	362	159	78	146	191
Sr	59.8	55.0	44.7	47.4	298	378	384	333
Co	2.51	2.18	2.14	1.48	45.3	50.9	44.4	50.0
Ni	1.34	2.04	1.87	1.69	189	213	168	194
Cu	4.28	12.10	2.60	2.14	12.5	12.2	13.7	64.8
Zn	20.4	14.2	28.9	15.6	123	120	108	144
Nb	13.7	9.78	13.6	12.1	16.4	14.4	16.2	17.2
Ba	414	205	229	323	3563	1726	2891	3693
Ta	2.30	1.73	1.87	1.81	1.50	0.94	1.03	1.16
Pb	56.6	62.4	54.9	56.0	34.9	13.9	28.7	46.5
Th	60.1	33.6	60.4	46.3	29.1	23.0	29.2	32.0
U	11.1	13.2	10.8	10.2	4.11	3.21	4.13	4.09
Zr	51.9	58.5	74.4	48.5	139	121	149	158
Hf	2.10	2.09	2.62	2.13	3.88	4.01	4.29	4.75
Y	21.3	12.7	21.4	16.1	22.6	24.7	24.1	25.6
Li	28.9	10.1	21.6	10.5	24.7	22.5	20.9	28.8
Be	3.00	2.06	2.50	3.36	1.37	1.16	1.46	2.92
Sc	5.16	3.86	5.10	4.17	26.0	31.8	26.9	29.8
V	14.4	9.57	14.9	13.8	219	262	226	245
Cr	4.76	3.19	4.97	4.49	506	585	489	563
Mo	1.02	1.75	0.96	0.54	0.13	0.20	0.14	0.13
Sb	0.64	1.43	0.62	0.76	0.36	0.58	0.43	0.53
Cs	8.67	15.70	7.35	8.11	36.5	23.7	29.6	24.2
W	3.41	1.09	3.44	2.41	1.39	2.47	2.23	3.30
Tl	2.97	2.64	3.41	3.14	2.82	1.32	2.45	3.14
La	68.5	30.6	69.5	42.5	88.8	82.2	91.4	99.4
Ce	128	56	131	79	138	133	142	154

Pr	14.2	6.34	14.6	8.94	13.9	14.2	14.4	15.6
Nd	50.2	23.0	51.3	32.0	48.2	50.8	49.1	53.1
Sm	8.82	4.12	8.92	5.83	7.13	7.80	7.31	7.80
Eu	0.72	0.50	0.61	0.54	1.59	1.89	1.70	1.82
Gd	6.76	3.16	6.70	4.43	6.16	6.78	6.64	6.81
Tb	1.05	0.55	1.16	0.71	0.95	1.13	1.05	0.96
Dy	4.64	2.45	4.68	3.16	4.37	5.26	4.50	4.84
Ho	0.70	0.45	0.76	0.53	0.81	0.86	0.85	0.83
Er	2.38	1.39	2.10	1.88	2.24	2.17	2.02	2.41
Tm	0.29	0.22	0.33	0.29	0.30	0.35	0.37	0.35
Yb	2.13	1.58	1.87	1.86	2.26	2.01	2.37	2.27
Lu	0.26	0.25	0.31	0.25	0.34	0.29	0.35	0.35

Note: LOI is loss on ignition.

747

748

749

750

751

752

753

754

755

38

TABLE 2. Representative major- and trace-element compositions of amphibole

Sample	HR2013-8										HR2013-10						HR2013-11	
Spot	s8	s23	s24	s26	s27	s35	s36	s42	s56	s59	s18	s19	s20	s21	s22	s23	s11	s17
Notes	mantle	core	rim	core	core	core	rim	core	core	rim	rim	core	core	core	core	core		
Oxide contents (wt %)																		
SiO$_2$	39.97	40.16	40.73	39.74	39.46	39.78	42.73	39.39	39.68	42.00	40.97	38.71	39.28	38.52	38.22	39.53	39.92	38.09
TiO$_2$	1.87	1.43	1.40	2.69	2.81	1.68	0.57	3.06	2.53	1.47	0.88	2.69	2.59	2.50	2.61	2.51	1.92	3.14
Al$_2$O$_3$	13.53	13.33	13.72	13.47	13.73	13.65	11.86	13.75	13.48	11.78	13.16	13.94	13.90	14.21	13.85	13.73	13.66	13.52
FeO	11.63	11.91	11.83	10.89	10.44	11.23	10.99	9.89	10.51	11.08	11.35	11.35	11.23	11.15	11.11	10.95	11.25	10.80
MnO	0.18	0.23	0.24	0.16	0.13	0.16	0.23	0.09	0.15	0.18	0.18	0.11	0.11	0.12	0.13	0.12	0.14	0.11
MgO	14.59	15.04	15.35	15.54	15.01	15.10	16.76	15.63	15.31	15.88	15.60	14.63	14.53	14.71	14.12	15.13	15.16	14.34
CaO	12.07	11.78	11.93	11.67	11.82	11.99	11.47	12.27	12.11	12.15	11.69	12.00	12.10	12.12	12.18	12.09	12.16	12.13
Na$_2$O	2.20	2.26	2.46	2.31	2.34	2.28	2.26	2.14	2.16	1.84	2.24	2.13	2.15	2.29	2.31	2.19	2.25	2.26
K$_2$O	0.88	0.74	0.83	0.85	0.93	1.05	0.74	1.39	1.09	0.77	1.05	1.24	1.30	1.27	1.25	1.21	1.21	1.09
F	b.d.l.	0.13	0.25	0.21	0.22	b.d.l.	0.27	b.d.l.	0.22	b.d.l.	b.d.l.	0.10	b.d.l.	b.d.l.	b.d.l.	b.d.l.	b.d.l.	b.d.l.
Cl	0.07	0.08	0.12	0.05	0.06	0.05	0.07	0.03	0.05	0.06	0.05	0.04	0.04	0.03	0.04	0.03	0.03	0.04
Total	96.98	96.99	98.72	97.48	96.83	96.95	97.83	97.62	97.18	97.19	97.16	96.87	97.21	96.92	95.82	97.48	97.69	95.51
Trace element contents (ppm)																		
P	367	146	222	208	292	204	230	131	193	178	168	207	202	150	147	178	180	158
V	414	320	308	432	457	332	206	477	407	328	280	424	435	464	437	455	395	416
Cr	9.74	91.5	148.5	5.03	10.5	15.9	180	171	14.8	34.4	90.7	41.3	23.0	18.0	12.3	13.5	178	198
Co	57.6	48.7	49.2	55.4	54.4	53.1	52.5	60.9	54.3	54.3	47.8	53.0	54.4	57.5	56.5	59.1	53.8	55.6
Ni	104	56.9	55.7	73.3	74.7	102	140	178	73.5	100	275	183	163	102	88.8	119	179	134
Cu	0.18	0.40	b.d.l.	0.25	0.25	0.07	0.17	0.26	0.41	0.29	0.20	0.32	0.27	0.25	0.57	0.03	0.37	0.30
Zn	88.3	85.5	83.7	54.1	51.8	65.8	87.0	41.8	56.5	78.6	84.2	56.2	55.3	54.7	52.0	49.9	52.8	40.5
Rb	7.90	4.63	3.60	4.72	5.98	6.73	4.73	8.54	8.74	5.29	7.65	7.53	8.80	14.29	13.00	10.09	9.45	6.09
Sr	633	485	537	585	645	455	398	599	519	481	390	497	508	519	493	523	459	513

Y	37.6	32.9	42.0	33.2	35.3	34.7	31.1	25.1	33.4	36.2	32.4	30.2	29.6	31.9	29.1	30.9	30.6	28.9
Zr	145	132	218	137	141	119	162	81	119	134	160	126	124	110	98	126	113	110
Nb	13.7	18.1	26.3	13.8	12.3	12.9	24.7	8.0	10.8	16.5	18.0	11.5	11.3	8.75	8.88	9.65	11.5	11.4
Mo	0.05	0.03	0.17	b.d.l.	b.d.l.	0.17	0.11	0.09	b.d.l.	0.13	0.28	0.05	0.08	0.03	0.11	b.d.l.	0.08	0.14
Cs	2.54	0.18	0.01	1.60	1.80	0.49	2.32	1.06	1.76	0.11	3.31	0.22	1.07	3.44	2.75	1.43	1.32	0.12
Ba	1068	750	782	927	1112	780	567	1679	1179	777	862	1433	1485	1521	1301	1407	1086	1151
La	42.8	47.2	41.7	25.3	37.7	34.2	40.6	23.7	29.3	38.2	54.6	32.9	31.8	27.2	23.4	27.1	29.7	21.9
Ce	116	132	122	76.8	104	103	116	69.4	87.8	110	143	90.6	89.5	77.2	67.5	76.1	83.7	64.1
Pr	15.2	16.6	16.1	10.5	13.9	13.3	14.3	9.16	11.6	14.8	16.9	11.9	11.6	10.5	9.31	10.4	11.2	8.95
Nd	65.5	64.8	66.9	48.2	59.1	58.1	56.6	41.9	52.9	61.4	66.6	53.1	50.8	47.0	42.0	45.8	50.4	41.0
Sm	12.6	10.9	11.6	10.1	12.9	11.4	8.8	8.2	10.8	11.5	9.9	10.4	10.0	9.7	8.8	9.8	9.5	8.3
Eu	3.49	3.18	3.33	2.85	3.15	2.75	2.67	2.37	2.74	3.14	2.75	2.48	2.83	2.74	2.29	2.44	2.82	2.24
Gd	10.7	8.41	10.4	9.18	10.6	8.60	6.58	7.67	9.00	8.95	7.64	7.82	8.47	7.88	7.48	8.28	8.15	7.90
Tb	1.39	1.00	1.30	1.25	1.29	1.05	0.95	0.93	1.11	1.21	0.97	1.11	1.07	1.05	1.05	1.11	1.10	1.01
Dy	7.56	6.09	7.81	6.41	7.89	7.09	5.38	6.04	6.64	6.97	5.08	5.96	6.11	6.23	5.77	5.92	6.17	5.72
Ho	1.27	1.20	1.59	1.08	1.43	1.30	1.06	0.88	1.23	1.32	1.09	1.13	1.09	1.22	1.02	1.14	1.14	0.95
Er	3.59	3.62	4.34	3.62	3.38	3.40	2.99	2.38	3.27	3.80	3.46	2.98	3.05	3.37	2.89	3.04	3.37	2.73
Tm	0.43	0.44	0.46	0.42	0.45	0.43	0.42	0.24	0.41	0.51	0.48	0.38	0.36	0.41	0.29	0.37	0.36	0.34
Yb	2.77	2.64	3.40	2.46	2.89	2.92	2.79	2.17	2.74	2.96	2.85	2.23	2.25	2.11	2.10	2.50	2.36	2.12
Lu	0.38	0.38	0.46	0.31	0.33	0.40	0.44	0.19	0.34	0.39	0.36	0.29	0.33	0.32	0.30	0.32	0.28	0.25
Hf	5.08	3.35	7.30	4.40	5.19	3.40	4.20	3.43	3.77	3.73	4.16	4.17	4.54	3.70	3.38	4.39	3.58	4.98
Ta	0.80	0.82	1.03	0.69	0.76	0.67	0.88	0.39	0.57	0.66	0.96	0.62	0.66	0.54	0.49	0.55	0.61	0.54
W	0.04	0.01	0.01	0.05	0.01	0.01	b.d.l.	b.d.l.	0.01	0.01	0.18	b.d.l.	0.03	0.46	b.d.l.	b.d.l.	0.01	0.05
Pb	4.81	5.32	5.78	4.13	5.12	4.36	4.40	3.63	4.22	5.18	4.24	3.98	4.12	4.70	4.38	3.66	4.56	3.50
Th	3.52	1.94	1.44	0.99	2.89	1.37	2.41	1.04	1.22	1.51	2.84	1.29	1.45	5.47	3.84	1.49	4.19	0.65
U	0.13	0.16	0.13	0.10	0.12	0.13	0.14	0.08	0.10	0.16	0.60	0.11	0.10	0.13	0.23	0.09	0.10	0.06

Note: b.d.l., below detection limit.

TABLE 3. Major -and trace-element compositions of actinolite

Sample				HR2013-8				
Spot	s10	s40	s41	s45	s48	s63	s64	s72
Oxide contents (wt %)								
SiO_2	54.22	55.96	56.01	54.73	55.14	55.80	55.41	55.49
TiO_2	b.d.l.	0.04	0.03	b.d.l.	0.04	b.d.l.	b.d.l.	b.d.l.
Al_2O_3	2.20	0.48	0.34	0.36	0.46	0.60	0.73	0.39
FeO	8.38	7.89	7.98	7.90	8.46	8.64	7.25	8.27
MnO	0.36	0.23	0.21	0.18	0.22	0.18	0.17	0.25
MgO	19.55	20.28	20.74	19.77	19.56	19.78	20.76	19.94
CaO	13.01	13.25	13.25	13.18	13.05	12.94	13.27	13.05
Na_2O	0.14	0.16	0.11	0.05	0.12	0.22	0.12	0.15
K_2O	0.06	0.02	0.02	0.01	0.03	0.04	b.d.l.	0.03
F	b.d.l.	b.d.l.	b.d.l.	b.d.l.	b.d.l.	b.d.l.	b.d.l.	b.d.l.
Cl	b.d.l.	0.01	b.d.l.	b.d.l.	b.d.l.	b.d.l.	b.d.l.	0.01
Total	97.91	98.31	98.69	96.19	97.07	98.19	97.70	97.55
Trace element contents								
(ppm)								
P	35.7	57.9	4.42	96.3	30.6	37.2	17.4	28.6
V	98.8	111	132	125	138	101	106	109
Cr	660	745	318	503	1060	352	586	263
Co	78.5	54.9	53.7	53.6	55.4	56.8	57.4	53.6
Ni	1034	883	845	880	524	691	711	872
Cu	0.10	0.43	0.05	0.11	0.08	0.05	0.21	b.d.l.
Zn	165	76.9	91.1	68.7	85.6	90.0	92.0	74.2
Rb	2.32	0.28	0.33	0.06	0.67	0.46	0.24	0.13
Sr	4.84	17.6	12.4	9.10	8.20	5.48	6.85	9.81
Y	0.25	0.73	0.15	0.48	0.48	0.71	0.53	0.19
Zr	1.51	4.65	7.43	0.52	4.74	7.23	3.81	0.68
Nb	0.04	0.03	b.d.l.	0.04	0.02	0.03	0.01	0.04
Mo	0.09	b.d.l.	b.d.l.	0.01	0.05	0.12	0.10	0.00
Cs	6.41	0.44	0.32	0.10	2.12	1.68	0.42	0.19
Ba	2.10	4.56	0.38	0.79	1.19	0.38	0.58	0.24
La	0.05	0.17	0.06	0.06	0.06	0.03	0.03	0.07
Ce	0.12	0.22	0.16	0.14	0.12	0.14	0.09	0.15
Pr	0.02	0.06	0.02	0.01	0.02	0.02	0.02	0.02
Nd	0.07	0.08	0.22	0.05	b.d.l.	0.09	0.10	0.03
Sm	b.d.l.	0.02	0.07	0.02	b.d.l.	0.04	0.02	b.d.l.
Eu	0.01	0.03	0.02	b.d.l.	0.01	0.01	0.01	b.d.l.
Gd	b.d.l.	0.09	0.02	b.d.l.	0.03	0.12	0.10	0.05
Tb	b.d.l.	0.03	b.d.l.	0.01	b.d.l.	0.01	0.01	b.d.l.

41

Dy	b.d.l.	0.14	0.04	0.03	0.05	0.07	0.07	0.01
Ho	0.01	0.02	0.01	0.01	0.02	0.02	0.01	0.01
Er	0.01	0.06	0.02	0.07	0.08	0.11	0.12	0.03
Tm	0.01	0.05	0.01	0.02	0.01	0.01	0.02	0.01
Yb	0.09	0.25	0.28	0.14	0.16	0.27	0.18	0.09
Lu	0.01	0.05	0.09	0.02	0.05	0.12	0.07	0.04
Hf	0.04	0.04	0.21	0.01	0.09	0.10	0.05	0.01
Ta	0.01	0.01	b.d.l.	0.01	0.01	b.d.l.	b.d.l.	0.01
W	0.07	b.d.l.	b.d.l.	b.d.l.	0.02	0.06	b.d.l.	0.01
Pb	0.81	0.67	0.27	1.64	3.99	0.41	0.41	0.18
Th	1.17	0.83	0.51	0.40	0.31	0.32	0.18	0.12
U	0.03	0.05	0.00	0.04	0.04	0.01	0.03	0.01

Note: b.d.l., below detection limit.

756

757

758

42

TABLE 4. Major-element compositions of Cr-spinel

Sample	HR2013-8				
Spot	s77	s78	s79	s81	s82
Oxide contents (wt %)					
SiO_2	0.07	0.07	0.06	0.08	0.07
TiO_2	0.76	0.89	0.78	0.84	0.80
Al_2O_3	19.36	22.02	18.78	19.78	19.42
FeO	26.33	29.03	32.79	28.23	28.73
MnO	0.40	0.47	0.97	0.45	0.49
MgO	10.89	9.83	6.92	9.73	9.42
CaO	0.05	b.d.l.	0.02	0.07	0.04
Cr_2O_3	40.54	36.89	39.46	39.38	40.19
Total	98.39	99.20	99.78	98.56	99.15

Note: b.d.l., below detection limit.
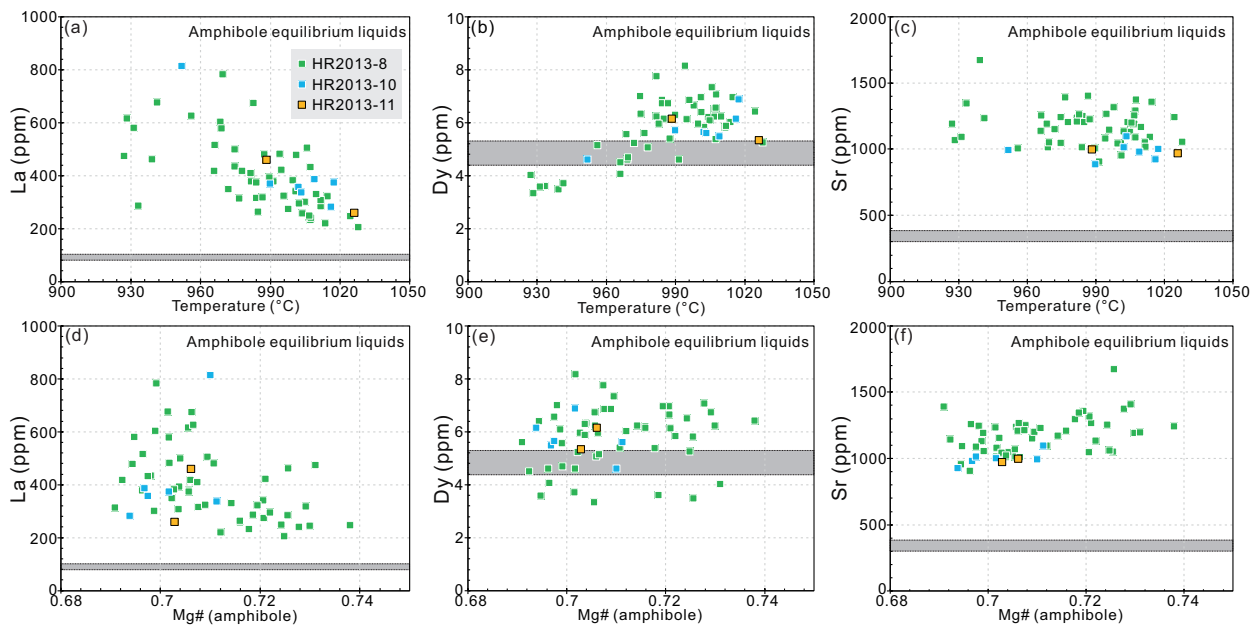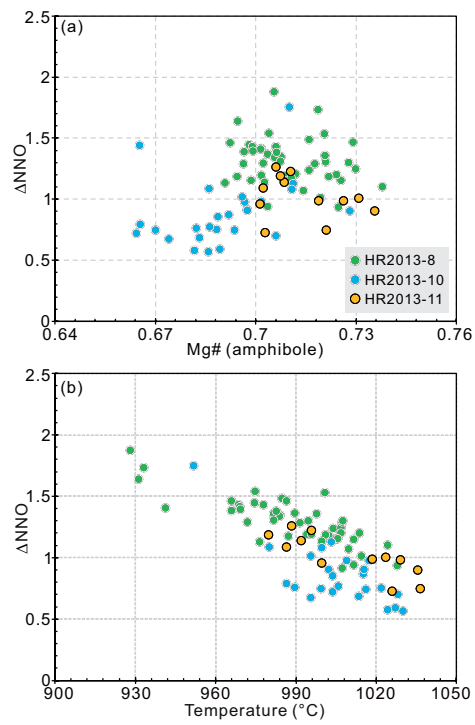
759

760

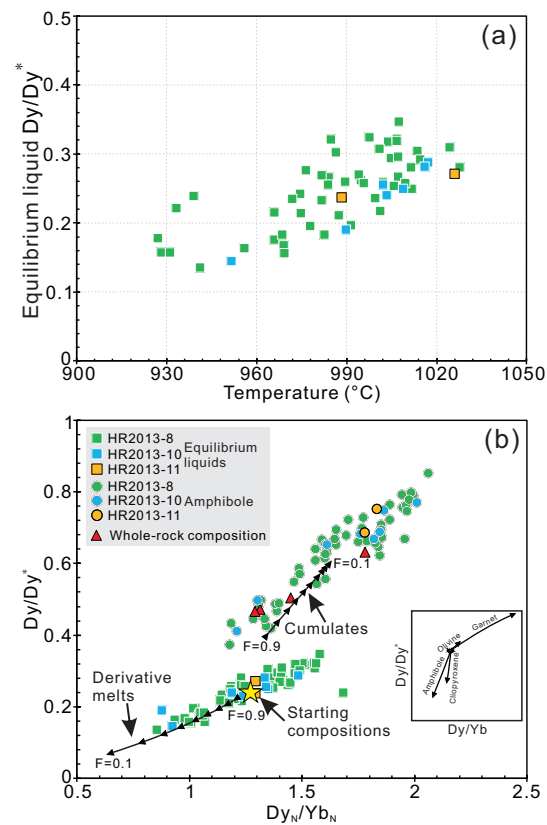761
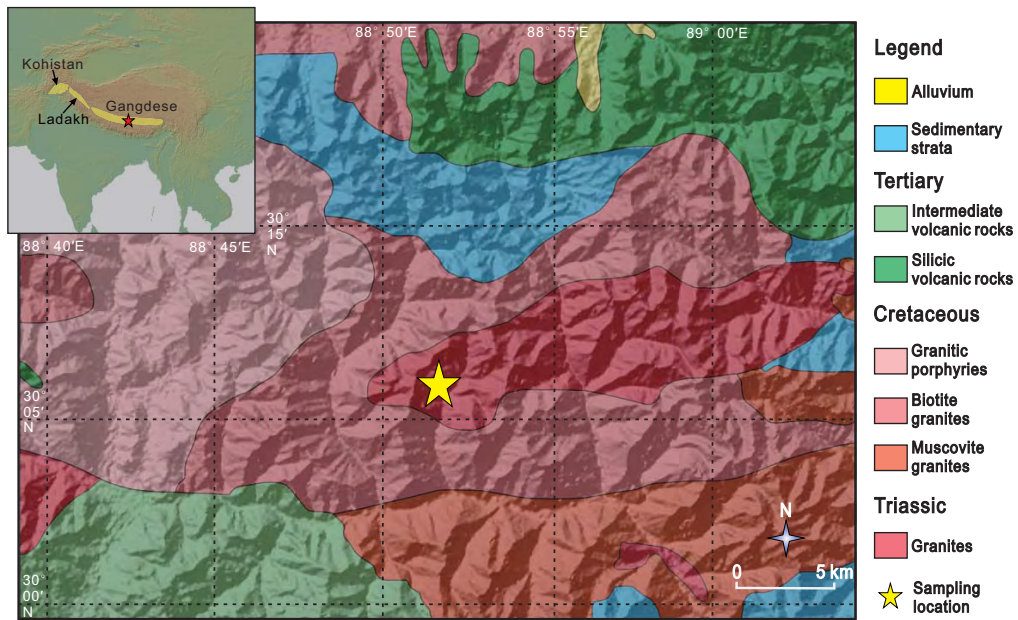
Figure 1
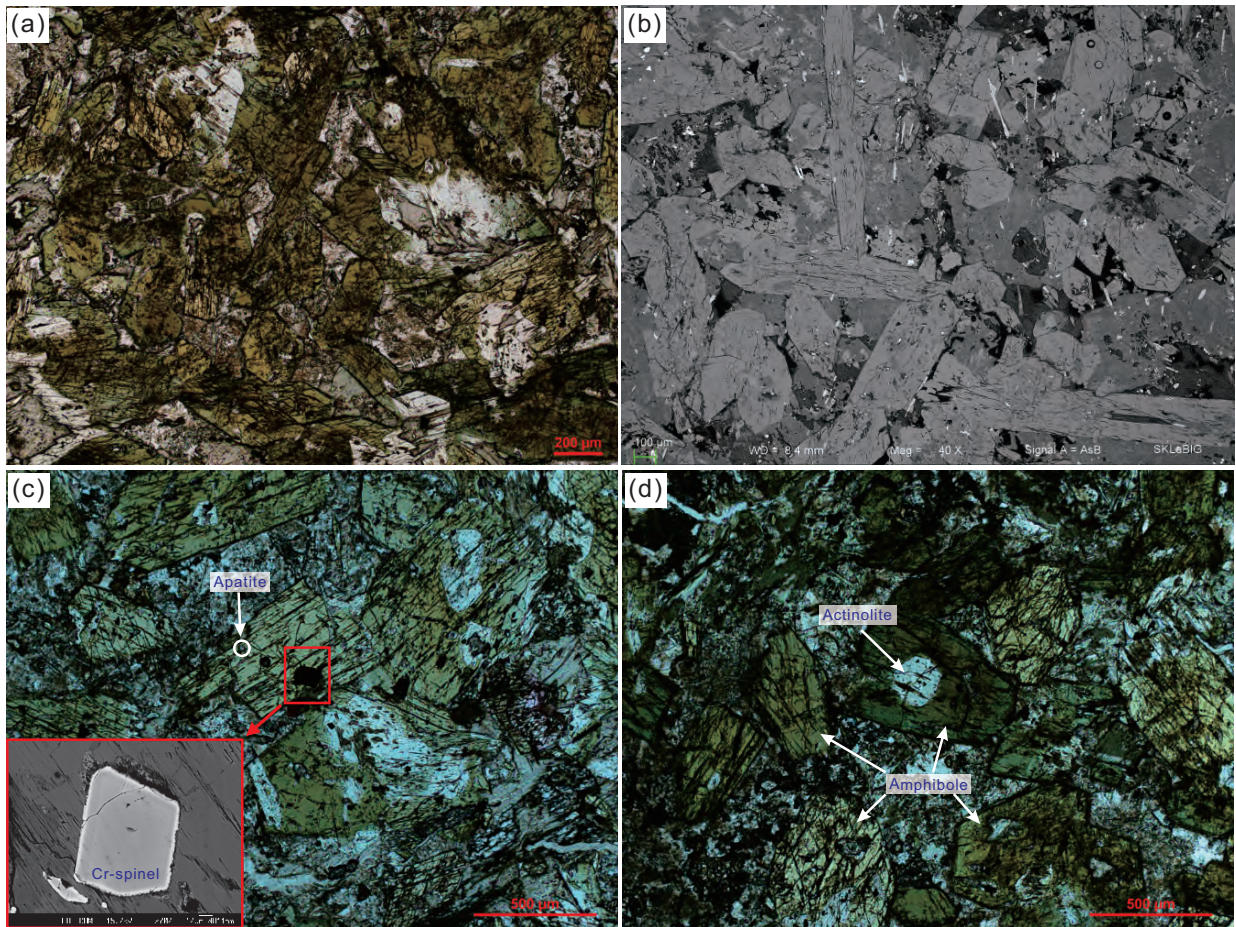
Figure 2
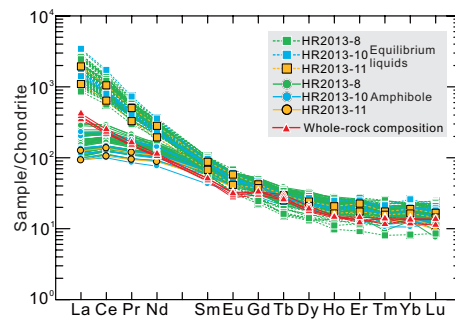
Figure 3
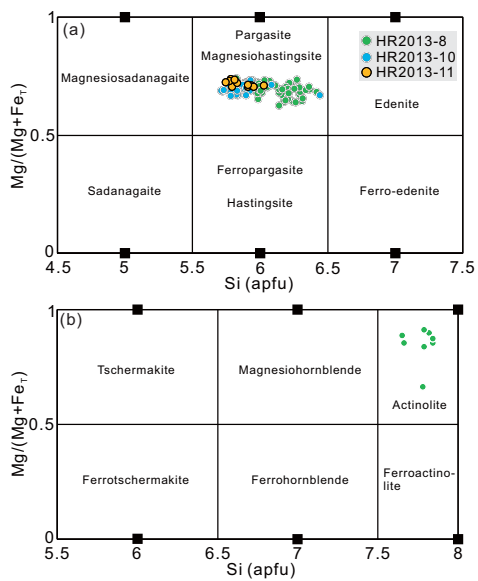
Figure 4
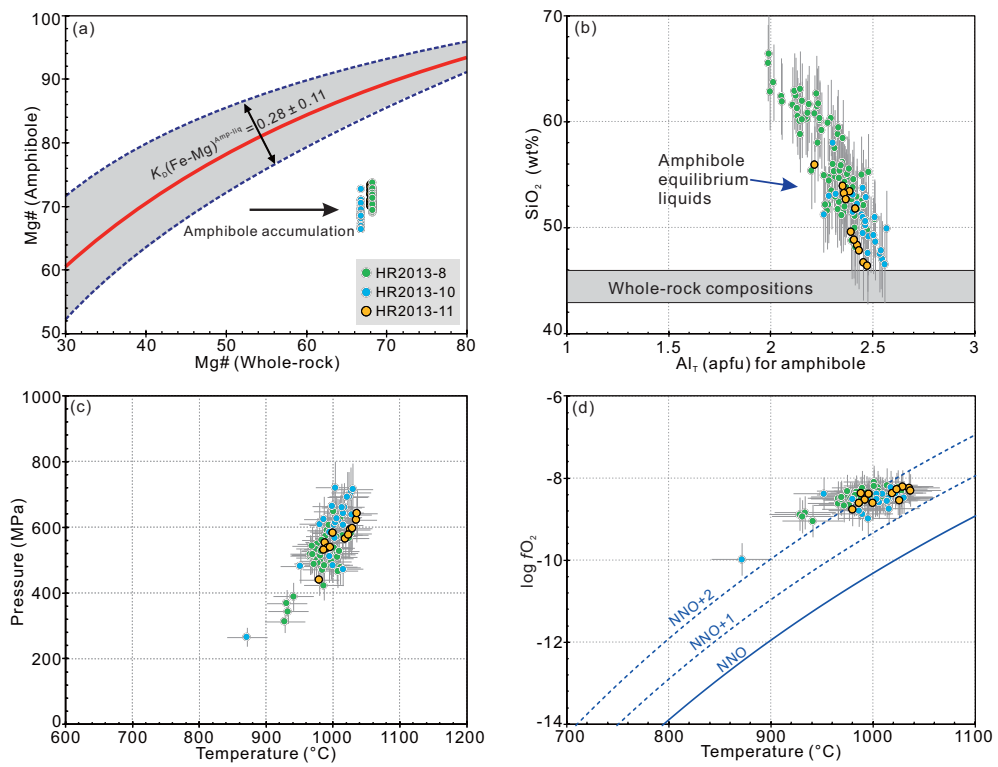
Figure 5
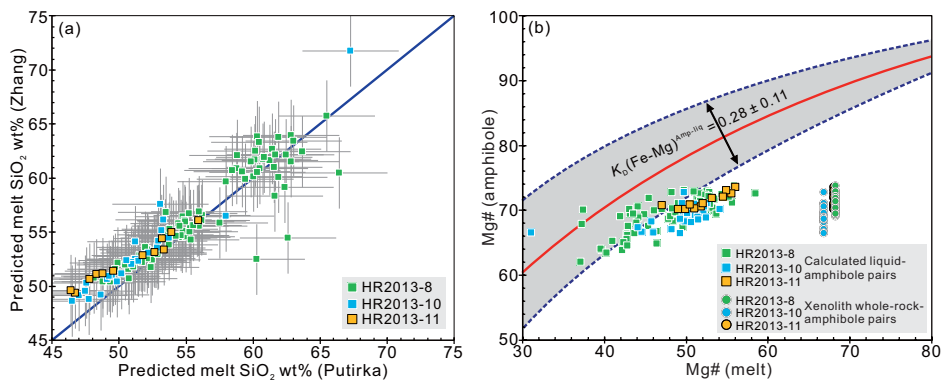
Figure 6
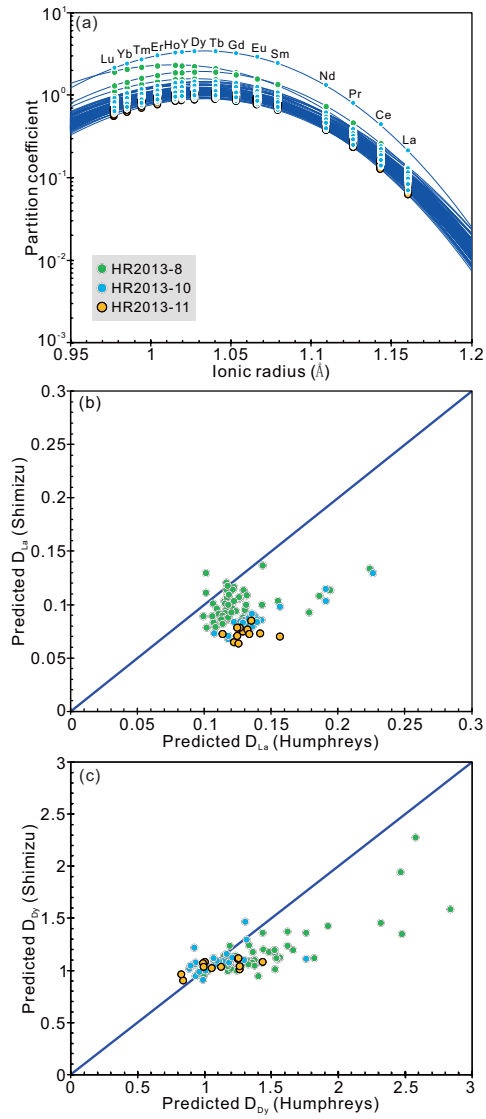
Figure 7

Figure 8

Figure 9

Figure 10